Pontifícia Universidade Católica
do Rio de Janeiro

Pedro Henrique Souza Calderano

Breakup of two-layer liquid films

Dissertação de Mestrado

Dissertation presented to the Programa de Pós–graduação em Engenharia Mecânica, do Departamento de Engenharia Mecânica da PUC-Rio in partial fulfillment of the requirements for the degree of Mestre em Engenharia Mecânica.

Advisor: Prof. Marcio da Silveira Carvalho

Rio de Janeiro
July 2021

Pontifícia Universidade Católica
do Rio de Janeiro

Pedro Henrique Souza Calderano

Breakup of two-layer liquid films

Dissertation presented to the Programa de Pós–graduação em Engenharia Mecânica da PUC-Rio in partial fulfillment of the requirements for the degree of Mestre em Engenharia Mecânica. Approved by the Examination Committee:

Prof. Marcio da Silveira Carvalho

Departamento de Engenharia Mecânica – PUC-Rio

Prof. Paulo Roberto de Souza Mendes
Departamento de Engenharia Mecânica – PUC-Rio

Prof. Roney Leon Thompson
Universidade Federal do Rio de Janeiro – UFRJ

Rio de Janeiro, July the 9th, 2021

Pedro Henrique Souza Calderano

Bachelor in Mechanical Engineering by Federal University of Juiz de Fora (2018)

Bibliographic data

Calderano, Pedro Henrique Souza

Breakup of two-layer liquid films / Pedro Henrique Souza Calderano; advisor: Marcio da Silveira Carvalho. – 2021.

67 f: il. color. ; 30 cm

Dissertação (mestrado) - Pontifícia Universidade Católica do Rio de Janeiro. Departamento de Engenharia Mecânica, 2021.

Inclui bibliografia

1. Engenharia Mecânica – Teses. 2. Filmes de duas camadas. 3. Revestimento por cortina. 4. Filmes finos. 5. Fluido viscoelástico. 6. Fluido não newtoniano. I. Carvalho, Marcio da Silveira. II. Pontifícia Universidade Católica do Rio de Janeiro. Departamento de Engenharia Mecânica.. III. Título.

CDD: 621

Acknowledgments

I would first like to thank my thesis advisor Prof. Marcio Carvalho. It was a pleasure to work with him. This work was only possible due to concepts and great discussions provided by Prof. Marcio. I am grateful for his guidance.

I would also like to thank Prof. Ivan Menezes. Prof. Ivan welcomed me to PUC-Rio and provided good support and advice in projects conducted through the length of this Master's degree.

I also highlight the importance of the support my parents and family offered me.

As good friends through this journey, Mateus Gheorghe, Rodolfo Teixeira, Renan Finotti, and Gabriela were the friends I spent most of my time with during the year I have lived in Rio.

I also thank the warm welcome from the LMMP members.

This study was financed in part by the Coordenação de Aperfeiçoamento de Pessoal de Nível Superior - Brasil (CAPES) - Finance Code 001.

Abstract

Calderano, Pedro Henrique Souza; Carvalho, Marcio da Silveira (Advisor). **Breakup of two-layer liquid films**. Rio de Janeiro, 2021. 67p. Dissertação de Mestrado – Department of Mechanical Engineering, Pontifical Catholic University of Rio de Janeiro.

Thin liquid sheets are present in a variety of systems and applications. Here, we are interested in double-layered sheets, which are common in the curtain coating process. In curtain coating, the liquid falls from a die forming a thin curtain before wetting the moving substrate. One of the most important process limits is the curtain breakup, which sets a lower limit for the coating liquid flow rate. Consequently, this flow rate lower limit defines the feasible minimum deposited film thickness. Experimental evidence have shown that using a two-layer curtain, with a viscoelastic thin layer, may delay the curtain breakup to lower flow ratios. The breakup of two-layer liquid sheets, composed of a Newtonian and a viscoelastic liquid, is studied by solving the differential equations that describe the evolution of the liquid sheet configuration until breakup. The effect of different parameters on the breakup time is determined. The results show the same behavior observed experimentally, thin viscoelastic liquid layer delays the breakup, stabilizing the liquid sheet.

Keywords

Double-layered sheets; Curtain coating; Thin-films; Viscoelastic fluid; Non-newtonian fluid.

Resumo

Calderano, Pedro Henrique Souza; Carvalho, Marcio da Silveira. **Quebra de um filme de líquido composto por duas camadas**. Rio de Janeiro, 2021. 67p. Dissertação de Mestrado – Departamento de Mechanical Engineering, Pontifical Catholic University of Rio de Janeiro.

Filmes finos de líquido estão presentes em uma variedade de sistemas e aplicações. Estamos interessados em filmes compostos por duas camadas, que são comuns no processo de revestimento por cortina. No revestimento por cortina, o líquido cai de uma matriz formando uma cortina formada por um filme fino antes de molhar o substrato em movimento. Um dos limites mais importantes do processo é a ruptura da cortina, que define um limite inferior para a vazão do líquido de revestimento. Consequentemente, este limite inferior da vazão define a espessura mínima viável do filme depositado. Evidências experimentais mostraram que o uso de uma cortina compostas por duas camadas, com uma das camadas sendo mais fina e viscoelástica, pode atrasar a ruptura da cortina para taxas de fluxo mais baixas. A quebra de filmes líquidos de duas camadas, compostas por um líquido newtoniano e um viscoelástico, é estudado por meio da resolução das equações diferenciais que descrevem a evolução da configuração do filme até seu rompimento. O efeito de diferentes parâmetros no tempo de ruptura é determinado. Os resultados mostram o mesmo comportamento observado experimentalmente, a fina camada de líquido viscoelástico retarda o rompimento, estabilizando o filme líquido.

Palavras-chave

Filmes de duas camadas; Revestimento por cortina; Filmes finos; Fluido viscoelástico; Fluido não newtoniano.

Table of contents

List of figures

List of tables

List of Abreviations

Greek symbols

α – oscillation wave number
$\dot{\gamma}$ – strain rate tensor
$\dot{\epsilon}$ – extension rate
η – non-Newtonian dynamic viscosity
η_0 – zero-extensional-rate viscosity
η_∞ – infinity-extensional-rate viscosity
η_p – polymer viscosity
η_s – solvent viscosity
η_r – non-dimensional viscosity coefficient
κ – surface curvature
λ – relaxation time
μ – dynamic viscosity
ρ – fluid density
σ – surface tension
τ – deviatoric stress tensor
$\mathbf{\Phi}$ – van der Waals potential
ω – oscillation growth rate

Roman symbols

A_{01} – Hamaker constant
A_{02} – Hamaker constant
A – capillary non-dimensional coefficient
D – viscous non-dimensional coefficient
De – Deborah number, non-dimensional coefficient
E – non-dimensional coefficient
F – non-dimensional coefficient
H – sheet thickness
h – non-dimensional thickness
$\mathcal{H}$ – ratio between layer thicknesses
K – initial viscosity ratio
k – non-dimensional coefficient
$\mathbb{L}$ – non-dimensional coefficient
L – sheet length
M – non-dimensional coefficient
N – non-dimensional coefficient

$\mathbf{n}$ – normal vector
p – isotropic pressure
S – van der Waals non-dimensional coefficient
$\mathbf{T}$ – fluid stress tensor
$\mathbf{t}$ – tangent vector
$\mathbf{u}$ – velocity vector
u – x-axis velocity
v – z-axis velocity
x – coordinate axis
z – coordinate axis

1
Introduction

A wide range of products from different industries takes advantage of liquid coating processes to enhance their functionality and quality. Thin film layers increase and modify the functionality of a bulk surface or substrate. They are used to protect surfaces from wear (mechanically functional), improve lubricity (mechanically functional), improve corrosion (chemically functional), and provide chemical resistance (chemically functional), provide diffusion barrier, optical properties, and many other functions. Although usually thin films do not affect the bulk properties of the material, they can completely modify the optical, electrical transport, and thermal properties of a surface, in addition to providing an enhanced degree of protection as well [1]. For instance, there are applications of coating technology ranging from biomedical materials to energy efficiency purposes, including laser optics, glazings and mirrors, thin-film batteries, thin-film fuel cells, semiconductor films, transparent electrical contacts, tribological coatings, and corrosion-resistant coatings. Besides the current relevance of the coating technologies on improved performance products, it has great potential to have even broader applications due to its potential to generate entirely new products and to improve the functionality of already existing ones [1].

Among the several coating processes, this study will concentrate on the process known as curtain coating. In curtain coating process, a liquid sheet is formed as the liquid exits the die and flows downwards in the form of a liquid curtain, before impinging the moving substrate, as sketched in Figure 1.1. Eventually, small wave-form perturbations will appear on the sheet's free surfaces. These disturbances may either evolve by increasing its amplitude until its size is large enough to breakup the sheet or be dissipated, leading to the curtain maintenance. The mentioned sheet breakup will lead to a defect in the fabrication process, which validates the rise of a wish for a better understanding of this phenomenon. Hence, in this study, we look upon the breakup process of free films.

1.1 Curtain coating process

Curtain coating is a premetered coating process at which the film thickness is set by the flow rate fed to the coating die and web speed. The liquid falls from the die forming a liquid curtain, before wetting the moving web or substrate. From the substrate perspective, it will receive its coating cover layer as soon as it passes under the curtain. Curtain coating enables high speed coating because it uses the liquid momentum to assist the wetting of the substrate, delaying air entrainment.

The coating sheet may be formed by a number of layers depending on desired product functionality. Hence, the liquid curtain may be formed by different layers, as illustrated in Figure 1.1. Curtain coating is challenging. Uniform thin liquid layer is only possible within a limited range of operating parameters. One important limitation of curtain coating is the liquid curtain breakup. The thickness range of the liquid curtain is on the micrometers scale. Then, any perturbation on the sheet surface may lead to the breakup of the liquid sheet. Therefore, the analysis of the liquid sheet breakup process is critical in the optimization and design of curtain coating.

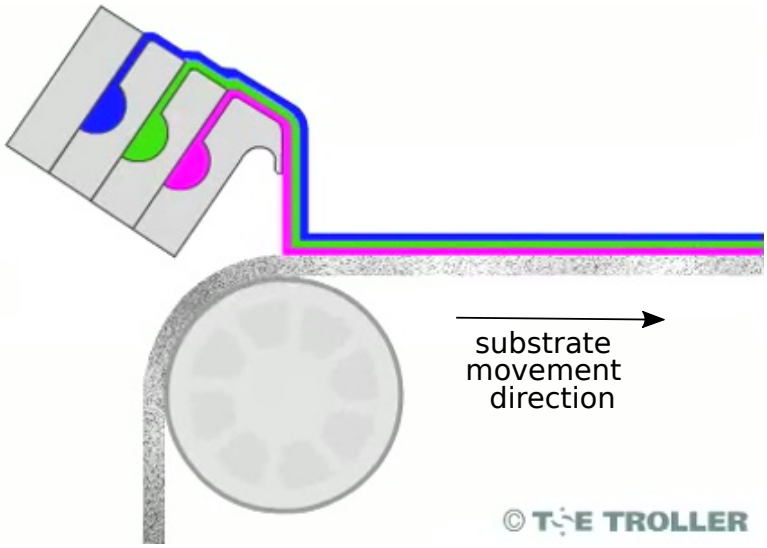

Figure 1.1: We can perceive in this picture a curtain coating scheme [2]. The coating liquid is pumped through a die and falls freely, establishing a curtain. At last, the coating surface reaches the moving substrate. It is noticeable in this image that the curtain sheet may be composed of multiple layers of fluid.

1.2 Sheet rupture

The evolution of surface configuration on thin fluid films has been a field of study for different applications such as coatings, adhesives, flotation, and

biological membranes to a host of areas in nanotechnology [3, 4]. Therefore, thin films have been investigated in a variety of conditions, such as on a substrate [5], in between substrates [6], and composed of one or more layers [7].

Here, the focus remains on the investigation of the breakup process of free films motivated by the curtain coating process. These films are susceptible to small perturbations on its surface since the interface between the liquid and the surrounding gas is a deformable boundary [3]. Brown [8] reported that the stability of a liquid curtain depends on the flow rate of coating material passing through the slot die. Additionally, he established a limit criteria by balancing a force proportional to the curtain's momentum with the surface tension force. Although some works found this limit accurate [9, 10], it was shown by different works that this stability criterion is not always accurate [11, 12].

The industry is pushing the breakup process knowledge further to meet aspirations of boosting coating speed and reducing the thickness of the liquid film [13] without hole formation and maintaining uniform thickness. In this regard, Eurnex and Davis [14] considered the Navier-Stokes equations for free films to derive its long-wave evolution equation and found a bifurcation point from where the stability of a curtain may be inferred. The proposed stability threshold only take into account surface tension and van der Waals forces. Following this work, Ida and Miksis [15] developed a numerical simulation to estimate the sheet rupture time, from a small amplitude perturbation to the sheet pinch-off. Among recent advances, Becerra et al. [16] used evidence from [17] that the effect of viscous forces may shift the breakup critical conditions to thinner curtains. Becerra's work experimentally shows the violation of Brown's rule [8] by the manipulation of viscosity using complex fluids. Stable and thinner liquid curtain is possible when the extensional viscosity effects of the coating polymer solution are strong.

Marston et al. [18] also presented an experimental investigation on the breakup of liquid curtains. They explored single and multi-layer sheets. This work gathers a significant amount of data, from which the authors show that the sheets formed obey the same rule for minimum flow rate definition. However, the hysteresis window varies according to the number of layers in the sheet.

Bazzi et al. [19] showed that the Eurnex and Davis' [14] stability indicator is valid not only for Newtonian fluids but also for complex fluids. Besides, the work concludes that although the viscoelastic forces do not account for deciding whether or not the curtain is stable, they have a great effect on sheet rupture

dynamics. Viscoelastic forces can significantly delay the breakup moment on unstable sheets when compared with the breakup time of Newtonian fluids.

Karim et al. [13] experimentally showed that two-layer sheets remained stable at significantly thinner thicknesses than single-layer sheets. Karim compared a double-layer curtain composed of a shear-thinning fluid bottom layer and a viscoelastic fluid top layer to a single-layer curtain constituted by a shear-thinning layer. The double-layer sheet was up to 60% thinner, depending on fluid properties. The authors acknowledge the viscoelastic top layer to be the main factor contributing to the slow down of the perturbation growth and consequently to the thickness reduction.

In this work, we aim to numerically model the breakup process of double-layered sheets and determine a relationship between viscosity characteristics and layer thicknesses and rupture time. The results can be used to design two layer curtain coating processes that enables the delay of sheet breakup to thinner curtains, allowing thin coatings.

2
Mathematical Formulation

This chapter presents the mathematical formulation that describes the flow in two-layer liquid sheets. Boundary conditions are applied at the interface between each layer and the surround gas phase and along the interface between the layers. Figure 2.1 illustrates the flow domain of interest, where each layer is represented by a different color. The flow is assumed two-dimensional, isothermal and incompressible.

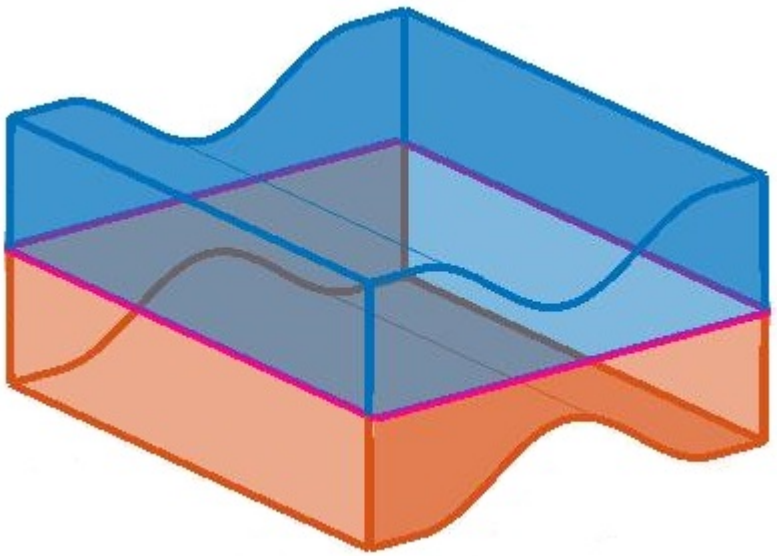

Figure 2.1: Sketch of the bilayer that composes the coating fluid sheet.

2.1 Coordinate system

The sheet is defined by two different layers of fluid forming three surfaces. One of those surfaces is the interface between both layers. The other two surfaces represent the boundaries of the liquid sheet.

To develop a mathematical model describing a liquid sheet made of assembled layers, the thickness dimension is labeled as z. We call the dimension that passes through the curtain extension as x. The x-axis is defined along one of the system's free-surfaces, as sketched in Figure 2.2. The direction perpendicular to z and $x-$axis is not considered since the flow is considered two-dimensional. Figure 2.2 represents the coordinate system described.

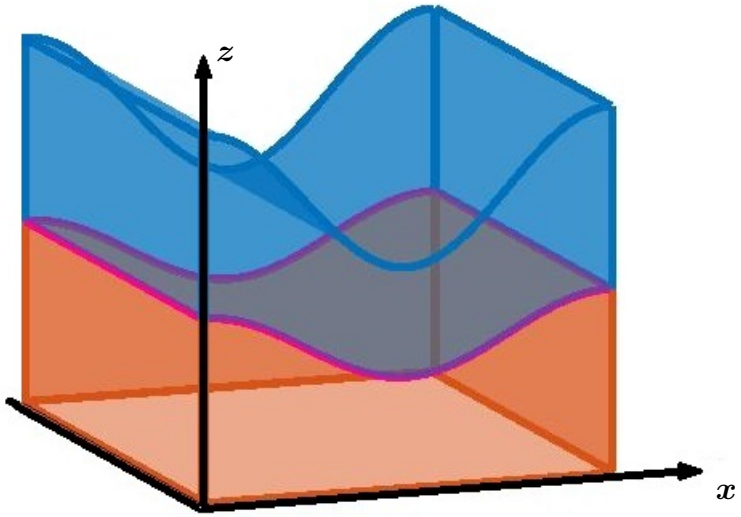

Figure 2.2: Sketch of the bilayer that composes the fluid sheet in a shifted coordinate system. For mathematical simplicity, the x-axis is defined as one of the gas-liquid borderlines. Therefore, in this adopted coordinate system, this border is represented as a flat line. All curvature that was from this gas-liquid surface is disseminated to the next surfaces.

2.2 Momentum and mass conservation equations

The fluid motion is described by the momentum and mass conservation equations.

For incompressible flow, the mass conservation equation is written as

$$\nabla \cdot \mathbf{u} = 0, \tag{2-1}$$

where $\mathbf{u}$ stands for the velocity vector.

Regarding the momentum conservation equation, it is essential to take in consideration every significant force in the system. As this problem has a thin dimension in thickness, the interactions between the interfaces represented by the van der Waals forces become important. It is an attractive force between the two boundary surfaces of a layer. This force is inversely proportional to the distance of the surfaces, then its relevance in the force balance increases as the film thickness reduces. Thereon, the momentum conservation equation is given by

$$\rho \frac{D}{Dt}\mathbf{u} = \nabla \cdot \mathbf{T} + \nabla \mathbf{\Phi}, \tag{2-2}$$

where ρ represents the fluid density, $\mathbf{T}$ is the stress tensor, and $\mathbf{\Phi}$ the van der Waals potential, which is defined as

$$\Phi = \frac{A}{h^3}, \tag{2-3}$$

where A is the Hamaker constant, which in this case relates two boundary sheets through a medium (coating fluid). h represents the layer thickness. As we have two layers, h is divided into h_1 and h_2, illustrated in Figure 2.3, which are respectively the thickness of the bottom layer and the total sheet thickness. Hence, the Equation (2-3) is written as

$$\Phi_1 = \frac{A_{01}}{h_1^3}, \tag{2-4}$$

for the bottom layer, and for the upper layer we have

$$\Phi_2 = \frac{A_{02}}{(h_2 - h_1)^3}. \tag{2-5}$$

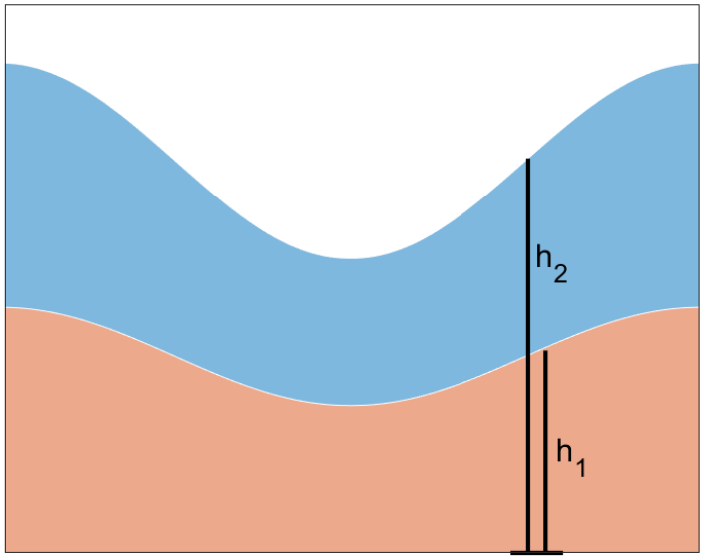

Figure 2.3: Sketch of the layers in a sheet. This image shows both layers and the layer height definition.

2.3 Constitutive equations

Constitutive equations or fluid models are mathematical statements that describe how the material deforms. Each model tries to describe the behavior of a certain class of fluids.

The description of the stress tensor conveniently splits it in a sum of two separate terms. The first of them is an isotropic part, and the last term is called extra stress or deviatoric stress tensor $\boldsymbol{\tau}$ associated with the fluid deformation.

$$\mathbf{T} = -p\mathbb{1} + \boldsymbol{\tau}. \tag{2-6}$$

The constitutive equations account for the deviatoric part of the stress tensor, $\boldsymbol{\tau}$, which is the term only affected by fluid deformation.

In this section, we present the constitutive equations used in this work. Subsection 2.3.1 discusses the Newtonian model, Subsection 2.3.2 the Generalized Newtonian Model (GNM), and Subsection 2.3.3 the Oldroyd-B model used to describe viscoelastic liquids.

2.3.1 Newtonian fluid

The Newtonian fluid model is the simplest mathematical model to describe how a fluid deforms when subjected to stress. It is a linear equation

in which stress is proportional to the rate of strain. The extra-stress tensor is written as

$$\boldsymbol{\tau} = \mu \left(\nabla \mathbf{u} + \nabla \mathbf{u}^T \right) + \left(\kappa - \frac{2\mu}{3} \right) (\nabla \cdot \mathbf{u}) \, \mathbb{1}, \tag{2-7}$$

where μ is the dynamic viscosity, and κ is the bulk viscosity. As we assume fluid incompressibility, the divergent operator $(\nabla \cdot \mathbf{u})$ is null. Then, the Equation (2-7) resumes as

$$\boldsymbol{\tau} = \mu \left(\nabla \mathbf{u} + \nabla \mathbf{u}^T \right). \tag{2-8}$$

2.3.2 Generalized Newtonian Model (GNM)

Often real fluids do not behave linearly. Therefore it is necessary to use a constitutive model that describes the non-linear behavior. Generalized Newtonian models are the constitutive equations in which stress is a function of strain rate, and there is no dependence on time. In these models the viscosity is not constant and vary with the deformation rate. They can be used to represent fluids in which an increase in strain rate reduces its viscosity, the so-called shear-thinning fluids. Also, they may be used to describe fluids in which the increment in strain rate results in a viscosity increase, known as shear-thickening fluids. The shear-thinning and the shear-thickening behaviors are represented in Figure 2.4.

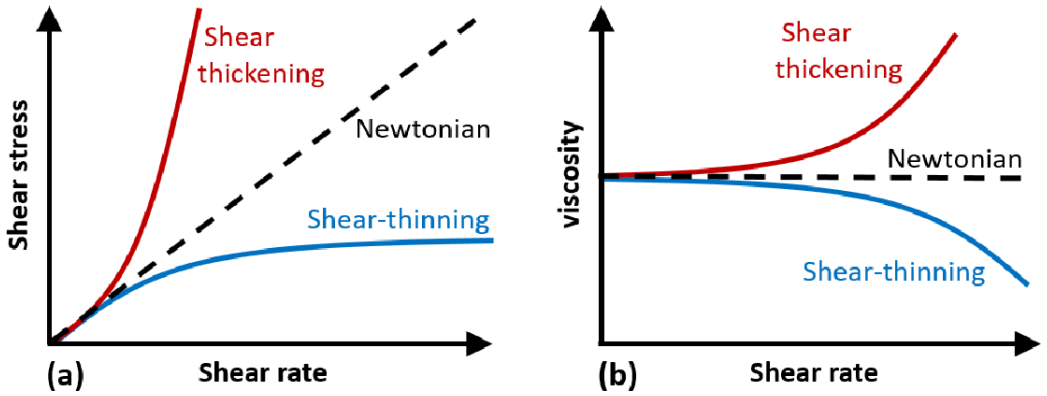

Figure 2.4: Sketch presenting a general perspective on the behavior of GNM fluids [20]. (a) It is noticeable that as the shear rate increases, the Newtonian fluid shear stress grows linearly. (b) The chart shows that Newtonian fluids have constant viscosity, shear-thickening fluids viscosity increase as the shear rate increases, and shear-thinning fluids viscosity have their viscosity reduced while the shear rate grows.

In the flow that occurs during the breakup of liquid sheets, the shear rate is negligible and the flow is dominated by planar extensional deformation. Moreover, polymer solutions' viscosity commonly increases as the extensional

strain increases [21]. This behavior is known as extensional-thickening. In an extensional flow, the deformation rate is called extension rate, $\dot{\epsilon}$.

There are a handful of GNMs available in the literature. Here, a simple GNM model is employed, the Carreau's model, which is stated as

$$\eta(\dot{\epsilon}) = \eta_\infty + (\eta_0 - \eta_\infty)\left(1 + (\lambda\dot{\epsilon})^2\right)^{\frac{n-1}{2}}, \tag{2-9}$$

where η_0 is zero-extensional-rate viscosity, η_∞ is infinity-extensional-rate viscosity, λ is a time constant, and n is the power-law index. As it was expressed in the previous paragraph, the growth in extension rate induces the rise of the viscosity, as it is shown in Figure 2.5.

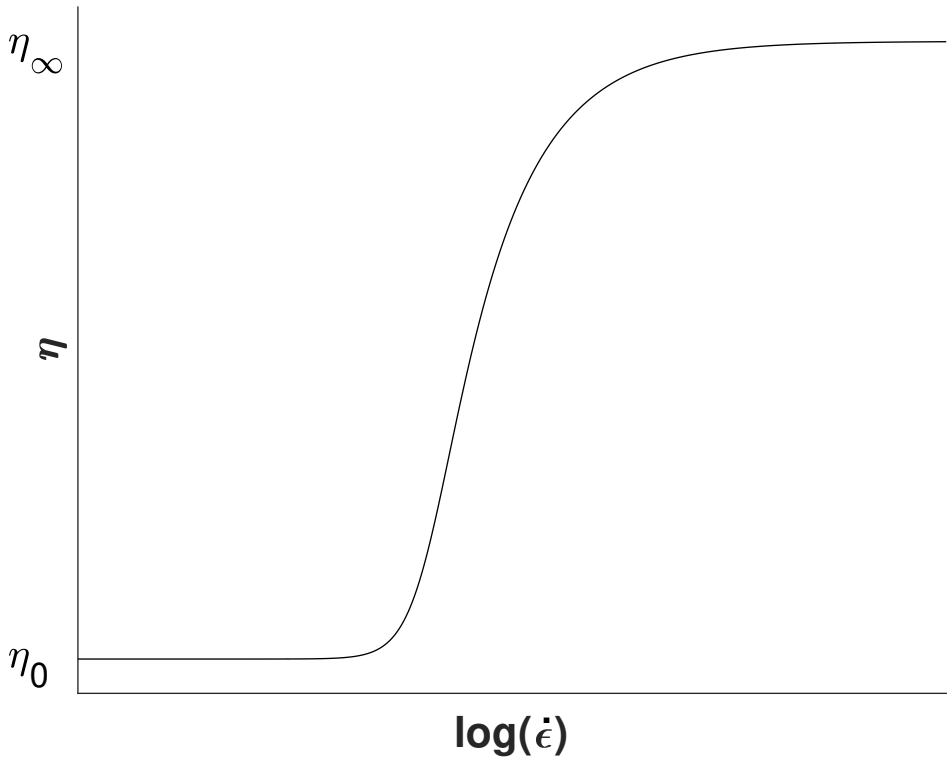

Figure 2.5: Sketch showing the Carreau model viscosity behavior in an extensional thickening circumstance. Regarding the model variables, in case of a change in the η_0 and η_∞ values, the response would change the initial and final viscosity plateaus respectively. As well as altering the λ value would shift the viscosity rise position. The increase in λ shifts the climb to the left, while its decrease shifts the climb to the right. The answer becomes a single plateau whether $\lambda \to 0$ or $\lambda \to \infty$, in which η will be $\eta = \eta_0$ or $\eta = \eta_\infty$ for every $\dot{\epsilon}$.

Finally, the stress tensor $\boldsymbol{\tau}$ is obtained from Equation (2-8), where the viscosity μ is replaced by the viscosity η calculated from Equation (2-9).

2.3.3 Oldroyd-B Model

The term viscoelastic means the coexistence of viscous, fluid-like, and elastic, solid-like, behavior in a material [21]. Further, it is possible to affirm that every material has a degree of viscoelasticity. The perception of viscoelasticity is a matter of time-scale. Every material has its natural time-scale. The viscoelastic properties are perceived when the flow time-scale matches the material time-scale, while the event will look-like only a fluid flow or a solid stretch when those time-scales are beyond comparison [21].

The linear viscoelasticity models are frequently used to describe the viscoelastic aspects of various materials. Each model has a different effect on how an input function affects stress and deformation responses with time. In this manner, the models describing the simplest material behavior are the Newtonian liquid and Hookean solid, representing the viscous liquid, no elastic recovery, and the glassy material, with complete elastic recovery. Further, there is the representation of the viscoelastic solid by the Kelvin-Voigt model, which shows the leathery behavior (slow full or partial elastic recovery). Also, the Maxwell model that describes viscoelastic liquid behavior, which is a rubbery flow. Here, the focus remains on the Maxwell model, which is the simplest model regarding viscoelastic liquids.

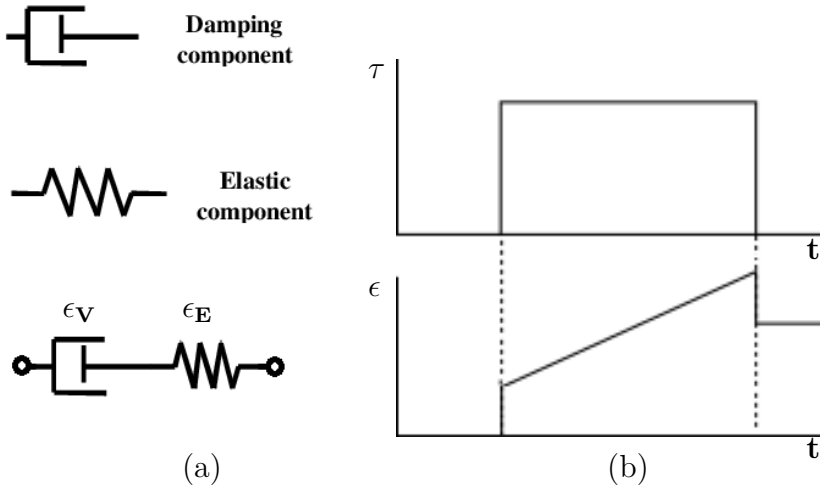

Figure 2.6: Visual concept of Maxwell model. (V - viscous component, E - elastic component). (a) Mechanical model of a Maxwell fluid. The stress over the damping and elastic component are shared ($\tau_V = \tau_E$), while deformation is the sum of deformations on the damping and elastic parts ($\epsilon = \epsilon_V + \epsilon_E$). (b) Deformation over time for a Maxwell viscoelastic fluid when a given imposed stress is applied.

The Maxwell viscoelastic model describes a viscoelastic liquid. It is represented by an association of a damping and an elastic component in

series. In a scenario of constant stress imposition, the deformation answer has an instantaneous step response and is continuously incremented until stress release. When stress is finally released, part of the total deformation retreats instantaneously, and the remaining deformation persists. The rapid deformation that appears in the moment of stress imposition and stress release are responses from the elastic component of the system, while the creep built among the instants of stress imposition and release comes from the damping component. Figure 2.6 summarizes the described Maxwell model. The following Equation (2-10) links deformation and stress through the derivation of the Maxwell model.

$$\boldsymbol{\tau} + \lambda \frac{\partial \boldsymbol{\tau}}{\partial t} = \eta \dot{\boldsymbol{\gamma}}, \tag{2-10}$$

where λ is the relaxation time, which is a time constant composed as the ratio between fluid viscosity and its elastic modulus. $\dot{\boldsymbol{\gamma}}$ is the deformation rate tensor. Although this model describes viscoelastic fluid behavior, it cannot be directly applied to provide stress for the equations in previous sections. That is because it does not follow the isotropy property [22], once this model will not hold the features displayed under coordinates rotation, i.e. the model is not frame invariant [22].

Oldroyd [23] derived a family of constitutive equations based on the linear viscoelastic models. Those Oldroyd models solve the mentioned obstacle. Such constitutive equations automatically satisfy the principle of material objectivity: a rigid-body rotation superimposed on any deformation history can not be registered by equations written in convected coordinates [24]. Oldroyd fluid models constitutive equations are written in convected coordinates, which Oldroyd introduced himself [25]. This coordinate system is convected or embedded. That is, the coordinate curves are attached to material particles and deform with the body [24]. The Oldroyd-B model comes from the mathematical development of Jeffreys fluid. However, in this section, it will be presented a simpler version of this model, derived from the Maxwell fluid. This simpler model is also known as the $upper - convected\ Maxwell\ fluid$. The adopted extra-stress tensor, $\boldsymbol{\tau}$, in the Oldroyd-B model is the sum of two components. The viscoelastic fluid is divided between a polymeric component and a solvent one. Therefore, the tensor is defined as $\boldsymbol{\tau} = \boldsymbol{\tau_p} + \boldsymbol{\tau_s}$, in which $\boldsymbol{\tau_p}$ is the tensor's polymeric component and $\boldsymbol{\tau_s}$ is the tensor's solvent component. The solvent component is defined as $\boldsymbol{\tau_s} = \mu_s \dot{\boldsymbol{\gamma}}$, where μ_s is the solvent viscosity. Equation (2-11) displays Maxwell Oldroyd's model

$$\boldsymbol{\tau_p} + \lambda \boldsymbol{\tau_p}^{\nabla} = \eta \dot{\boldsymbol{\gamma}}, \tag{2-11}$$

where $\dot{\boldsymbol{\gamma}}$ is the strain rate tensor, λ is the relaxation time, and the convected

derivative is defined as

$$\boldsymbol{\tau}^{\boldsymbol{\nabla}} = \frac{D}{Dt}\boldsymbol{\tau} - \boldsymbol{\nabla}\mathbf{u}\cdot\boldsymbol{\tau} - \boldsymbol{\tau}\cdot\boldsymbol{\nabla}\mathbf{u}. \tag{2-12}$$

Considering that this work addresses an extensional flow, we briefly analyze the viscosity behavior in extensional flow under the Oldroyd-B constitutive model. Extensional flows behave differently from classical shear flows because they act toward compressibility since they elongate the fluid. As liquids are considered either uncompressible or having low compressibility rates, viscosity under extensional flows, known as elongational viscosity (η_E), is higher than the viscosities measured in shear flows. Considering a planar extension, elongational viscosity is measured as $\tau_{11} - \tau_{22} = \dot{\epsilon}\eta_E(\dot{\epsilon})$ [21], where τ_{11} and τ_{22} are the stresses in the first and second principal directions, and $\dot{\epsilon}$ is the elongation rate. A common dimensionless notation form for the elongational viscosity is the Trouton ratio, defined as a relation between elongational and shear viscosities, $Tr = \eta_E/\eta$ [21].

The Oldroyd-B model suggests that the extensional stress growth depends on a dimensionless time and a dimensionless extension rate [26]. Nguyen et al. [27] showed that the Oldroyd-B model is reasonable to predict behavior for an M1 fluid in an extensional flow under constant extension rates. In this work [27] plots the apparent elongational viscosity (η_E) vs. time and the obtained Trouton ratio vs. a dimensionless time, as exposed in Figures 2.7 and 2.8. Figure 2.7 shows that the elongational viscosity changes with time although the elongation rate is constant. Within the data range available in the plot, elongational viscosity η_E increases as time passes. It is also perceptible that the increase in elongation rate $\dot{\epsilon}$ induces an increase in the apparent elongational viscosity. Figure 2.8 shows the plot for non-dimensionalized parameters. It allows noticing that the relaxation time λ affects the viscosity η_E as well. Fluids with higher λ experience higher apparent viscosity than fluids with lower λ under the same extension rate $\dot{\epsilon}$.

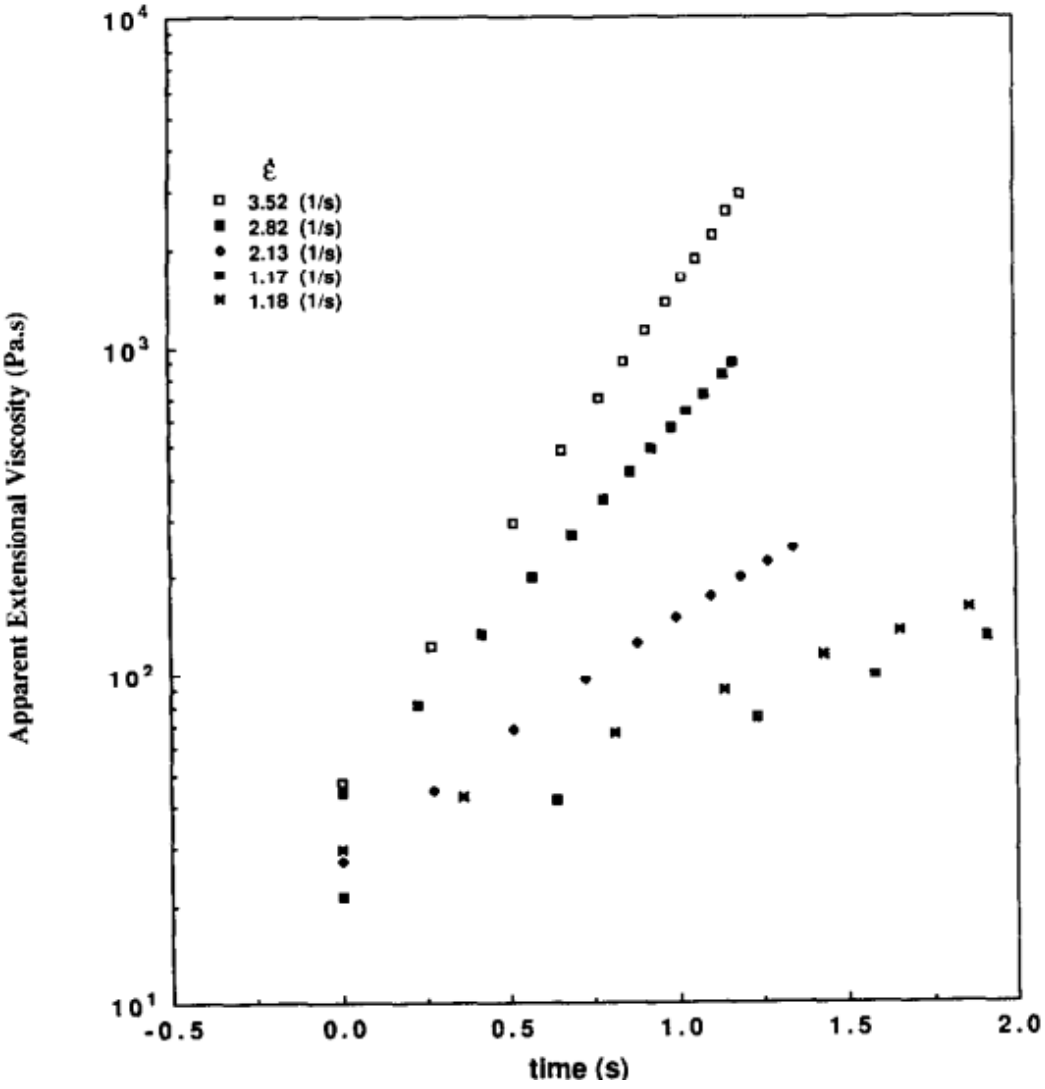

Figure 2.7: Plot of elongational viscosity (η_E) vs time for a M1 fluid modeled by the Oldroyd-B model [27].

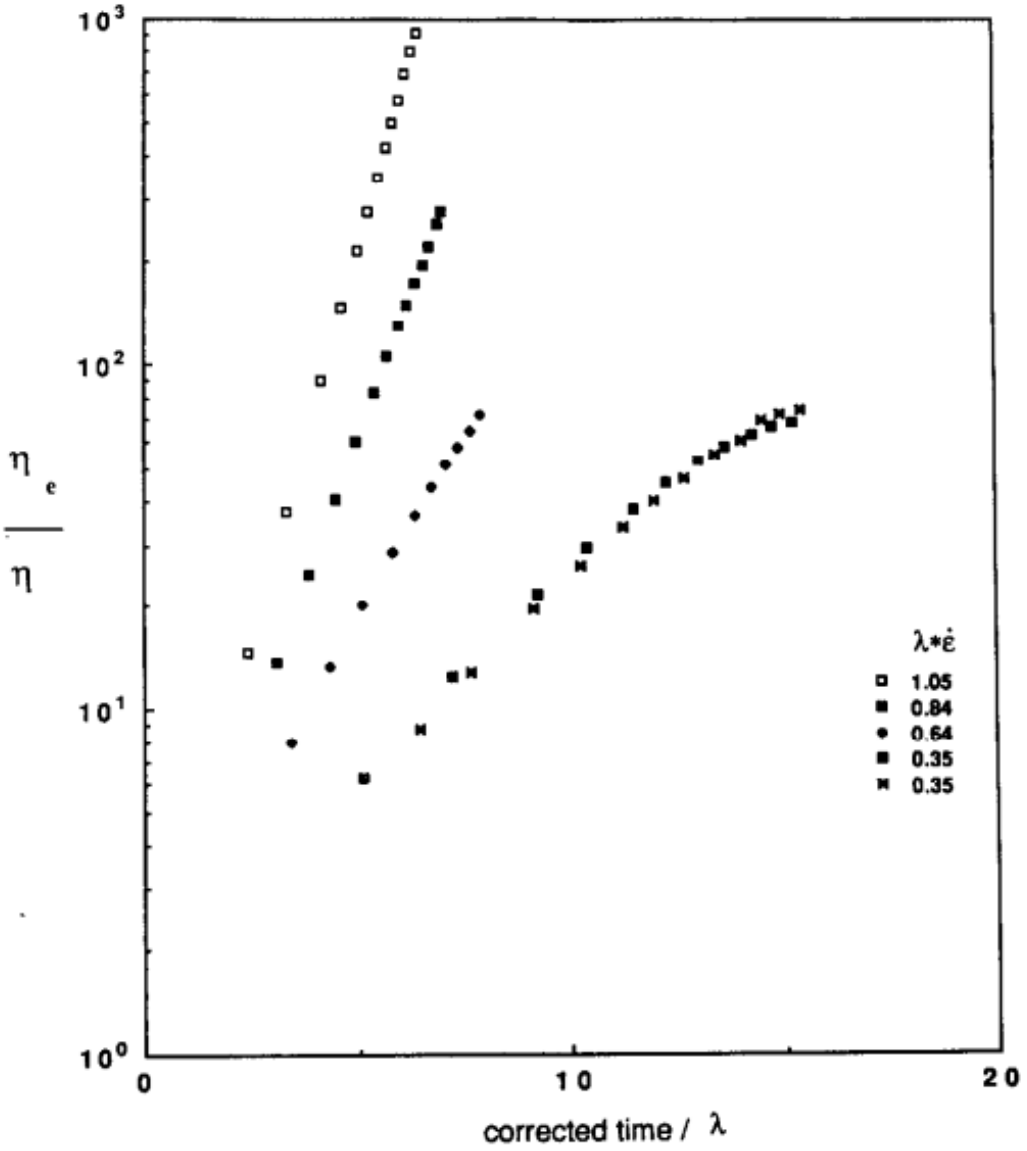

Figure 2.8: Plot of $\ln(\eta_e/\eta)$ vs $(corrected\ time/\lambda)$ for a M1 fluid modeled by the Oldroyd-B model [27].

2.4 Boundary conditions

To complete the mathematical formulation, we need to define the boundary and initial conditions. The boundary conditions define the effects of the ambient gas on the free-surface and the effect of one layer on the other one.

In this problem, the boundary conditions are defined in terms of the normal and tangential forces acting along the flow boundaries. Figure 2.9 shows schematically in a drawing the vectors indicating those directions. Hence, to calculate the boundary conditions, it is necessary to perform dot products between the direction vectors and the stress tensor.

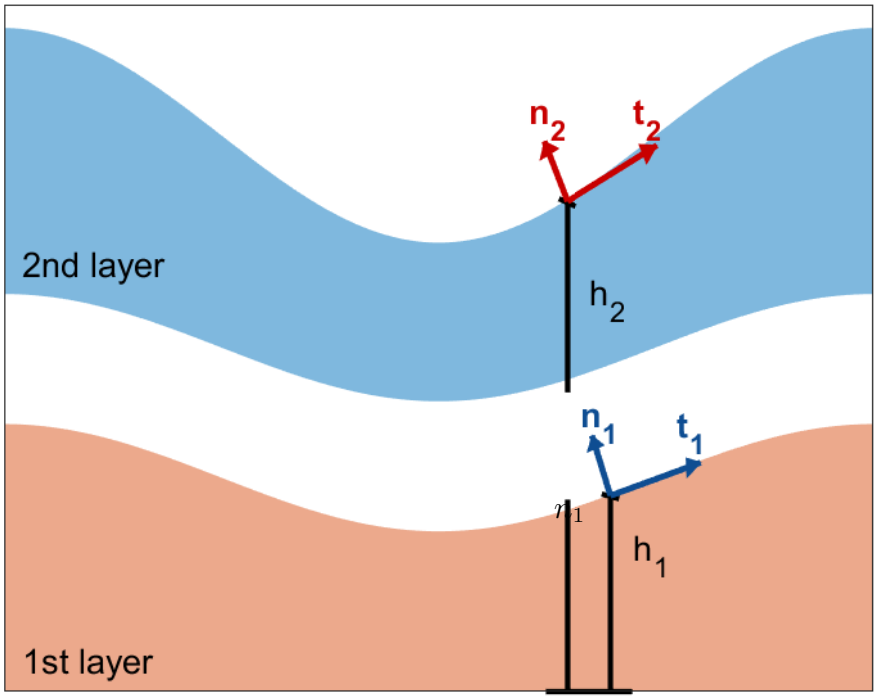

Figure 2.9: Sketch of the layers in a sheet. This image shows both layers detached from each other. It shows the vectors in those surfaces that indicate normal, $\boldsymbol{n}$, and tangential, $\boldsymbol{t}$, directions. The directions given by those vectors are useful to calculate the forces acting as boundary conditions in the problem. It also clarifies the thickness dimensions adopted in the formulation.

Regarding the direction vectors, they can be defined as

$$\boldsymbol{n} = \left[\frac{\partial h}{\partial x}\ \widehat{\boldsymbol{i}};\quad -1\ \widehat{\boldsymbol{j}}\right]\left(1+\left(\frac{\partial h}{\partial x}\right)^2\right)^{-1/2}, \tag{2-13}$$

and

$$\boldsymbol{t} = \begin{bmatrix} 1\ \widehat{\boldsymbol{i}}; & \dfrac{\partial h}{\partial x}\ \widehat{\boldsymbol{j}} \end{bmatrix} \left(1 + \left(\frac{\partial h}{\partial x}\right)^2\right)^{-1/2}, \tag{2-14}$$

where $\boldsymbol{n}$ and $\boldsymbol{t}$ are the normal and tangential vectors respectively. h is $h = h_1(x)$ or $h = h_2(x)$, which corresponds to the layer surface height in the z-axis, depending on the layer the vector refers to. Due to sheet slenderness, the approximation $(\partial h/\partial x)^2 \longrightarrow 0$ is adopted.

The force acting in a point on a surface is obtained by the dot product between its stress tensor and its normal vector. The dot product between the resulting vector and a direction vector results in the modulus of the force in that direction. Therefore, the boundary conditions along the top interface, in $z = h_2$, are given by the normal and tangential stress balance:

$$\begin{aligned} &\boldsymbol{n_2} \cdot \boldsymbol{\tau} \cdot \boldsymbol{n_2} = \sigma\kappa \Longrightarrow \\ &-p_2 + \tau_{zz2} - 2\tau_{xz2}\frac{\partial h_2}{\partial x} = \sigma\kappa, \ \textit{and} \end{aligned} \tag{2-15}$$

$$\begin{aligned} &\boldsymbol{t_2} \cdot \boldsymbol{\tau} \cdot \boldsymbol{n_2} = 0 \Longrightarrow \\ &\frac{\partial h_2}{\partial x}\left(\tau_{xx2} - \tau_{zz2}\right) - \tau_{zx2} = 0. \end{aligned} \tag{2-16}$$

u and v represents components of the velocity vector $\boldsymbol{u}$ in the axis x and z. σ is surface tension and κ stands for the surface curvature defined as the norm of the tangent unit vector derivative [28]:

$$\kappa = \frac{\partial^2 h}{\partial x^2}\left(1 + \left(\frac{\partial h}{\partial x}\right)^2\right)^{-1/2}. \tag{2-17}$$

The index 2 indicates that the variable is evaluated at the sheet's 2^{nd} layer.

The boundary conditions between the two layers, in $z = h_1$, are given by

$$\begin{aligned} &\boldsymbol{n_2} \cdot \boldsymbol{\tau} \cdot \boldsymbol{n_2} = \boldsymbol{n_1} \cdot \boldsymbol{\tau} \cdot \boldsymbol{n_1} \Longrightarrow \\ &-(p_1 - p_2) + \left[\tau_{zz1} - 2\tau_{zx1}\frac{\partial h_1}{\partial x}\right] - \left[\tau_{zz2} - 2\tau_{zx2}\frac{\partial h_2}{\partial x}\right] = 0, \end{aligned} \tag{2-18}$$

and

$$\begin{aligned} &\boldsymbol{t_1} \cdot \boldsymbol{\tau} \cdot \boldsymbol{n_1} = \tau_s = K\left(u_1 - u_2\right) \Longrightarrow \\ &\frac{\partial h_1}{\partial x}\left(\tau_{xx1} - \tau_{zz1}\right) - \tau_{zx1} = K\left(u_1 - u_2\right). \end{aligned} \tag{2-19}$$

The index 1 indicates that the variable is evaluated at the sheet's 1^{st} layer. τ_s is the shear stress between the two layers. It is modeled here as a simple relation between the average velocity of each layer, K is proportional between the initial fluid viscosities, for simplicity we take $K = \mu_2/\mu_1$.

Lastly, there is the kinematic condition, Equation (2-20), which bounds the surface movement to velocity in the layer. This condition assures that the

boundary $h = h(x)$ is moving accordingly to the flow.

$$\boldsymbol{n} \cdot \boldsymbol{u} = \left(\frac{\partial h}{\partial t}\right) \Longrightarrow \frac{\partial h}{\partial t} + u\frac{\partial h}{\partial x} = v. \tag{2-20}$$

2.5 Long-wave approximation (Asymptotic expansion)

The long-wave approximation adopted uses an asymptotic expansion that takes advantage of the long and thin geometry of the problem, and the flow symmetry in each layer [19, 29, 30]. The equations presented in the previous sections of this chapter are simplified by expanding of the variables in a power series and then neglecting the high-order terms. The exploited symmetry permits truncating some of the terms in the series depending on function parity regarding the variable. Even variables only present even coefficients while odd variables only present odd coefficients, as it is expressed in Equations (2-21).

$$\begin{aligned}
u\left(x,z,t\right) &= U_0 + U_2 z^2 + ... \\
v\left(x,z,t\right) &= V_1 z + V_3 z^3 + ... \\
p\left(x,z,t\right) &= P_0 + P_2 z^2 + ... \\
\phi\left(x,z,t\right) &= \phi_0 + \phi_2 z^2 + ... \\
\tau_{xx}\left(x,z,t\right) &= T_{xx0} + T_{xx2} z^2 + ... \\
\tau_{xz}\left(x,z,t\right) &= T_{xz1} z + T_{xz3} z^3 + ... \\
\tau_{zz}\left(x,z,t\right) &= T_{zz0} + T_{zz2} z^2 + ...
\end{aligned} \tag{2-21}$$

Due to the thin thickness of the layers, $z \ll 1$, higher-order z terms are truncated as the equations are developed. Also, we perform the simplification $z \longrightarrow h(x)$ to the remaining terms that are multiplied by z, since this long-wave supposes plug flow and the forces acting on the system, besides viscous forces, depend on the sheet's thickness.

2.6 System of equations

The long-wave approximation simplifies the conservation equations into a system of 1-D transient partial differential equations. The development of the system is discussed in Subsection 2.6.1. Then, Subsection 2.6.2 states the adopted non-dimensionalization relations. Finally, Subsections 2.6.3, 2.6.4, and 2.6.5 presents the final system of equations. The indexes ① and ② are used to indicate from which layer the variable refers.

2.6.1 System development

The system describing the sheet dynamics is developed using the conservation equations and the boundary conditions. The path used to develop this system is described in this Subsection.

We first write the mass and moment conservation equations, Equations (2-1) and (2-2), for the first layer.

$$\frac{\partial u_1}{\partial x} + \frac{\partial v_1}{\partial z} = 0, \tag{2-22}$$

and the moment conservation

$$\rho_1 \left(\frac{\partial u_1}{\partial t} + u_1 \frac{\partial u_1}{\partial x} + v_1 \frac{\partial u_1}{\partial z} \right) = \left(\frac{\partial \tau_{xx1}}{\partial x} + \frac{\partial \tau_{zx1}}{\partial z} \right) - \frac{\partial P_1}{\partial x} - \frac{\partial \phi_1}{\partial x}. \tag{2-23}$$

For the second liquid layer, the equations are analogous

$$\frac{\partial u_2}{\partial x} + \frac{\partial v_2}{\partial z} = 0, \tag{2-24}$$

and the following moment conservation equation

$$\rho_2 \left(\frac{\partial u_2}{\partial t} + u_2 \frac{\partial u_2}{\partial x} + v_2 \frac{\partial u_2}{\partial z} \right) = \left(\frac{\partial \tau_{xx2}}{\partial x} + \frac{\partial \tau_{zx2}}{\partial z} \right) - \frac{\partial P_2}{\partial x} - \frac{\partial \phi_2}{\partial x}. \tag{2-25}$$

We consider the boundary condition equations, Equations (2-15), (2-16), (2-18), and (2-19). And finally, the kinematic boundary condition, Equation (2-20), which becomes

$$\boldsymbol{n} \cdot \boldsymbol{u} = \left(\frac{\partial h}{\partial x} \right) \Longrightarrow \frac{\partial h_1}{\partial t} + u_1 \frac{\partial h_1}{\partial x} = v_1, \tag{2-26}$$

considering the first layer of fluid, and

$$\boldsymbol{n} \cdot \boldsymbol{u} = \left(\frac{\partial h}{\partial x} \right) \Longrightarrow \frac{\partial h_2}{\partial t} + u_2 \frac{\partial h_2}{\partial x} = v_2 \tag{2-27}$$

considering the second layer of fluid.

The development of equations for the second layer is as follows. The pressure from Equation (2-15) is isolated as shown in Equation (2-28),

$$-P_0^{②} = \sigma\kappa - T_{zz0}^{②} \Longrightarrow -\frac{\partial P_0^{②}}{\partial x} = \sigma \frac{\partial \kappa}{\partial x} - \frac{\partial T_{zz0}^{②}}{\partial x} \tag{2-28}$$

and substituted into momentum conservation equation, Equation (2-25), for its development. We can isolate the term τ_{zx1} presented in Equation (2-16), as reported in Equation (2-29). So, we use it to transform the term τ_{zx1} from momentum conservation into τ_{xx0} and τ_{zz0}.

$$T_{zx1}^{②} z = \frac{\partial h_2}{\partial x} \left(T_{xx0}^{②} - T_{zz0}^{②} \right) \tag{2-29}$$

We use mass conservation, Equation (2-24), to transform the velocity component v into the velocity component u, as stated in Equation (2-30).

$$V_1^{②} = -\frac{\partial U_0^{②}}{\partial x} \tag{2-30}$$

The kinematic boundary condition, Equation (2-27), is also developed using mass conservation, Equation (2-30), so the PDE is only function of the u component of fluid velocity and sheet height.

$$\frac{\partial h_2}{\partial t} + U^{②}\frac{\partial h_2}{\partial x} + h_2\frac{\partial U^{②}}{\partial x} = 0 \tag{2-31}$$

Therefore, momentum conservation and kinematic boundary condition equations remain in the developed system. The equations regarding the first layer of the sheet are developed in a similar manner. It will be also developed the momentum conservation and kinematic boundary condition equations, Equations (2-23) and (2-26), using Equations (2-18), (2-19), and (2-22). The intermediate results achieved using the those relationships are Equations (2-32), (2-33), and (2-34).

$$V_1^{①} = -\frac{\partial U_0^{①}}{\partial x} \tag{2-32}$$

$$-T_{zx1}^{①} z = K\left(U_0^{①} - U_0^{②}\right) - \frac{\partial h_1}{\partial x}\left(T_{xx0}^{①} - T_{zz0}^{①}\right) \tag{2-33}$$

$$\frac{-\partial P_0^{①}}{\partial x} = \sigma\frac{\partial \kappa}{\partial x} - \frac{\partial T_{zz0}^{①}}{\partial x} - 2K\left(U_0^{①} - U_0^{②}\right)\frac{\partial^2 h_1}{\partial x^2} - 2K\left(\frac{\partial U_0^{①}}{\partial x} - \frac{\partial U_0^{②}}{\partial x}\right)\frac{\partial h_1}{\partial x} \tag{2-34}$$

It is adopted $(\partial h/\partial x)^2 \longrightarrow 0$, $z^2 \longrightarrow 0$, and $\kappa \approx \partial^2 h_2/\partial x^2$. Lastly, it is necessary to apply the stress tensor equation of the selected fluid model, Equation (2-8) for the newtonian fluid model, Equation (2-9) for the GNM fluid model, or Equation (2-11) for the viscoelastic fluid model. The fully developed systems are presented in the Subsections 2.6.3, 2.6.4, and 2.6.5.

2.6.2 Non-dimensionalization

Dimensionless variables, represented by *, are defined as:

$$U^* = U\frac{\rho_2 L}{\mu_2}, \quad t^* = t\frac{\mu_2}{L^2\rho_2}, \quad h^* = \frac{h}{H}, \quad x^* = \frac{x}{L}, \quad \tau^* = \tau\frac{\rho^2 L}{\mu_2^2},$$

in which L refers to sheet length and H to sheet thickness.

From now on, all variables displayed are non-dimensional. Therefore, we hide the * symbol.

2.6.3 Newtonian system

Equation I

$$\frac{\partial h_1}{\partial t} + U^{①}\frac{\partial h_1}{\partial x} + h_1\frac{\partial U^{①}}{\partial x} = 0 \tag{2-35}$$

Equation II

$$\begin{aligned}&\frac{\partial U^{①}}{\partial t} + U^{①}\frac{\partial U^{①}}{\partial x} - 3S_1\frac{\partial^3 h_2}{\partial x^3} - 4D\frac{\partial^2 U^{①}}{\partial x^2} - \\ &4D\frac{1}{h_1}\frac{\partial h_1}{\partial x}\frac{\partial U^{①}}{\partial x} + 2k\frac{\partial^2 h_1}{\partial x^2}\left(U^{①} - U^{②}\right) + \\ &+ 2k\frac{\partial h_1}{\partial x}\left(\frac{\partial U^{①}}{\partial x} - \frac{\partial U^{②}}{\partial x}\right) + \mathbb{L}\frac{1}{h_1}\left(U^{①} - U^{②}\right) - \frac{3}{16}A_1\frac{1}{h_1^4}\frac{\partial h_1}{\partial x} = 0\end{aligned} \tag{2-36}$$

Equation III

$$\frac{\partial h_2}{\partial t} + U^{②}\frac{\partial h_2}{\partial x} + h_2\frac{\partial U^{②}}{\partial x} = 0 \tag{2-37}$$

Equation IV

$$\begin{aligned}&\frac{\partial U^{②}}{\partial t} + U^{②}\frac{\partial U^{②}}{\partial x} - 3S_2\frac{\partial^3 h_2}{\partial x^3} - 4\frac{\partial^2 U^{②}}{\partial x^2} - \\ &- 4\frac{1}{h_2}\frac{\partial h_2}{\partial x}\frac{\partial U^{②}}{\partial x} - \frac{3}{16}A_2\frac{1}{(h_2 - h_1)^4}\left(\frac{\partial h_2}{\partial x} - \frac{\partial h_1}{\partial x}\right) = 0\end{aligned} \tag{2-38}$$

in which

$$\begin{aligned}S_1 &= \frac{\sigma H\rho_2^2}{6\mu_2^2\rho_1}, & S_2 &= \frac{\sigma H\rho_2}{6\mu_2^2},\\ D &= \frac{\mu_1\rho_2}{\rho_1\mu_2},\\ k &= \frac{K\rho_2 H}{\rho_1\mu_2},\\ \mathbb{L} &= \frac{K\rho_2 L^2}{H\rho_1\mu_2},\\ A_1 &= \frac{A_{01}\rho_2^2 L^2}{6\pi H^3\mu_2^2\rho_1}, & A_2 &= \frac{A_{02}\rho_2 L^2}{6\pi H^3\mu_2^2},\end{aligned}$$

are the non-dimensional parameters of the problem.

Equations I and III, Equations (2-35) and (2-35) on the described Newtonian system, remain unchanged on other fluid systems. Therefore, all systems share those equations. However, in case of any modification on the fluid model, Equations II and IV need adjustment.

2.6.4 GNM system

Equation II

$$\frac{\partial U^{①}}{\partial t} + U^{①}\frac{\partial U^{①}}{\partial x} - 3S_1\frac{\partial^3 h_2}{\partial x^3} - 4D\frac{\partial^2 U^{①}}{\partial x^2} - 4D\frac{1}{h_1}\frac{\partial h_1}{\partial x}\frac{\partial U^{①}}{\partial x} - \\ - 4N\frac{\partial \eta_1}{\partial x}\frac{\partial U^{①}}{\partial x} + 2k\frac{\partial^2 h_1}{\partial x^2}\left(U^{①} - U^{②}\right) + 2k\frac{\partial h_1}{\partial x}\left(\frac{\partial U^{①}}{\partial x} - \frac{\partial U^{②}}{\partial x}\right) + \\ + \mathbb{L}\frac{1}{h_1}\left(U^{①} - U^{②}\right) - \frac{3}{16}A_1\frac{1}{h_1^4}\frac{\partial h_1}{\partial x} = 0 \tag{2-39}$$

Equation IV

$$\frac{\partial U^{②}}{\partial t} + U^{②}\frac{\partial U^{②}}{\partial x} - 3S_2\frac{\partial^3 h_2}{\partial x^3} - 4M\frac{\partial^2 U^{②}}{\partial x^2} - 4M\frac{1}{h_2}\frac{\partial h_2}{\partial x}\frac{\partial U^{②}}{\partial x} - \\ - 4G\frac{\partial \eta_2}{\partial x}\frac{\partial U^{②}}{\partial x} - \frac{3}{16}A_2\frac{1}{(h_2 - h_1)^4}\left(\frac{\partial h_2}{\partial x} - \frac{\partial h_1}{\partial x}\right) = 0 \tag{2-40}$$

in which,

$$N = \frac{\rho_2}{\rho_1\mu_2}, \qquad M = \frac{\eta_2}{\mu_2},$$

$$\eta\left(\dot{\gamma}\right) = \eta_\infty + \left(\mu_2 - \eta_\infty\right)\left(1 + \left(\widetilde{\lambda}\left[2\frac{\partial U^{②}}{\partial x}\right]\right)^a\right)^{\frac{n-1}{a}} \Longrightarrow$$

$$\frac{\partial \eta}{\partial x} = \left(\mu_2 - \eta_\infty\right)\left[\left(n-1\right)\left(1 + \left(2\widetilde{\lambda}\frac{\partial U^{②}}{\partial x}\right)^a\right)^{\frac{n-1-a}{a}} \right. \\ \left. \left(2\widetilde{\lambda}\frac{\partial U^{②}}{\partial x}\right)^{a-1}\left(2\widetilde{\lambda}\frac{\partial^2 U^{②}}{\partial x^2}\right)\right],$$

$$\widetilde{\lambda} = \frac{\lambda\mu_2}{L^2\rho_2},$$

where μ_2 is the perceived viscosity when there is no extensional stress, $\widetilde{\lambda}$ is the Carreau number, and η_∞ is the perceived viscosity when extensional stress is considerably high. The constants a and n are established in this work as $a = 2$ and $n = 0.5$.

2.6.5 Oldroyd-B system

The Oldroyd-B system present two additional equations that describe the evolution of the polymeric component of the stress tensor.

Equation II

$$\frac{\partial U^{①}}{\partial t} + U^{①}\frac{\partial U^{①}}{\partial x} - 3S_1\frac{\partial^3 h_2}{\partial x^3} - 4D\frac{\partial^2 U^{①}}{\partial x^2} - 4D\frac{1}{h_1}\frac{\partial h_1}{\partial x}\frac{\partial U^{①}}{\partial x} -$$
$$- E\left(\frac{\partial \tau_{xx}^{①}}{\partial x} - \frac{\partial \tau_{zz}^{①}}{\partial x}\right) - E\frac{1}{h_1}\frac{\partial h_1}{\partial x}\left(\tau_{xx}^{①} - \tau_{zz}^{①}\right) + 2k\frac{\partial^2 h_1}{\partial x^2}\left(U^{①} - U^{②}\right) +$$
$$+ 2k\frac{\partial h_1}{\partial x}\left(\frac{\partial U^{①}}{\partial x} - \frac{\partial U^{②}}{\partial x}\right) + \mathbb{L}\frac{1}{h_1}\left(U^{①} - U^{②}\right) - \frac{3}{16}A_1\frac{1}{h_1^4}\frac{\partial h_1}{\partial x} = 0 \tag{2-41}$$

Equation IV

$$\frac{\partial U^{②}}{\partial t} + U^{②}\frac{\partial U^{②}}{\partial x} - 3S_2\frac{\partial^3 h_2}{\partial x^3} - 4\frac{\partial^2 U^{②}}{\partial x^2} - 4\frac{1}{h_2}\frac{\partial h_2}{\partial x}\frac{\partial U^{②}}{\partial x} - L\left(\frac{\partial \tau_{xx}^{②}}{\partial x} - \frac{\partial \tau_{zz}^{②}}{\partial x}\right) -$$
$$- L\frac{1}{h_2}\frac{\partial h_2}{\partial x}\left(\tau_{xx}^{②} - \tau_{zz}^{②}\right) - \frac{3}{16}A_2\frac{1}{(h_2 - h_1)^4}\left(\frac{\partial h_2}{\partial x} - \frac{\partial h_1}{\partial x}\right) = 0 \tag{2-42}$$

Equation V

$$De\frac{\partial \tau_{xx}}{\partial t} = -\tau_{xx} - De\,u\frac{\partial \tau_{xx}}{\partial x} + 2De\,\frac{\partial u}{\partial x}\tau_{xx} + 2\eta_r\frac{\partial u}{\partial x} \tag{2-43}$$

Equation VI

$$De\frac{\partial \tau_{zz}}{\partial t} = -\tau_{zz} - De\,u\frac{\partial \tau_{zz}}{\partial x} - 2De\,\frac{\partial u}{\partial x}\tau_{zz} - 2\eta_r\frac{\partial u}{\partial x} \tag{2-44}$$

in which the non-dimensional parameters are:

$$E = \frac{\rho_2 L}{\rho_1}, \qquad De = \frac{\lambda\eta_s}{L^2\rho_2}.$$

2.7
Boundary and initial conditions

The system of equations described in the last section is developed from a restricted space frame and from an initial configuration. As it is discussed in the next chapter, the equations are first order and parabolic regarding time. On the other hand, with respect to the spacial variable, it is second order and elliptical. Considering that, the equations system boundary conditions are presented in the following paragraphs.

The initial condition corresponds to the vectors set as the initial configuration in time $t = 0$, which are f^0. The velocity and stress vectors, $\boldsymbol{u}_j^0$, $\boldsymbol{\tau}_{xx_j}^{\ 0}$ and $\boldsymbol{\tau}_{zz_j}^{\ 0}$, are initially arrays of zeros. It assumes that the fluid is not moving in any particular direction. The vector which represents the surfaces, $\boldsymbol{h}_j^0$, are initialized with the addition of a height value plus a small deviation, so it is possible to observe how the system evolves from this perturbed configura-

tion. This starting deviation is a cosine wave, where the deviation amplitude is $\epsilon_0 = 2\%$ of the sheet's height, as demonstrated in Figure 2.10.

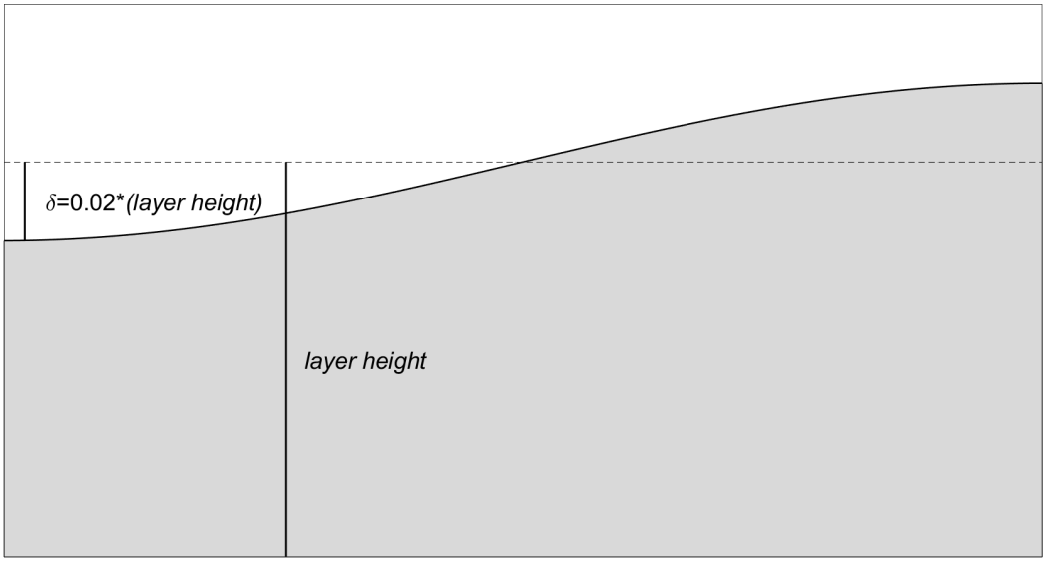

Figure 2.10: Sketch of initial surface position. It is started with a constant height value plus a cosine wave deviation of amplitude $\epsilon_0 = 2\%(layer\ height)$.

The space boundary conditions are present in both space extremes of the simulated system. Hence, those boundaries are applied in the points $x = 0$ and $x = L$ and must be held in every time iteration. In $x = 0$, the boundaries are the Dirichlet boundary condition $u = 0$, and the Neumann boundary conditions $\partial h/\partial x = 0$, $\partial \tau_{xx}/\partial x = 0$, and $\partial \tau_{zz}/\partial x = 0$. In $x = L$, we have the Dirichlet boundary condition $u = 0$, and the Neumann boundary conditions $\partial h/\partial x = 0$, $\partial \tau_{xx}/\partial x = 0$, and $\partial \tau_{zz}/\partial x = 0$. The implementation of those boundaries guided the answer evolution through the time grid according to the theoretical structured behavior.

2.8 Linear stability analysis

Linear stability analysis allows a broad perception of flow stability. This analysis is a mathematical procedure that starts at the differential equations and results in an expression stating whether the system is stable or if an imposed perturbation grows. Then, the final expression provides a chart from which we can explore a range of system configurations while aware of its stability. Considering that, this section is dedicated to the linear stability analysis development of the elaborated system.

Previous works have carried linear stability analysis for single-layered sheets. Erneux et al. [14] have shown that only the ratio between the capillary and van der Waals forces determine flow behavior. Following, Bazzi et al. [19] added the analysis of viscoelastic fluid flow. Here, we further exploit the subject addressing the stability analysis for non-Newtonian double-layered sheets. This analysis will be valuable to simulate sheets under different initial conditions.

The equations presented in Section 2.6 accept a steady-state solution where the fluid velocity is null, as consequence fluid flow is absent, the stress tensor stays constant, and the surface configuration remains unchanged in both layers. This solution is added of a tiny perturbation, represented by

$$\begin{aligned}\left(h_2, U^{②}, \tau_{xx}^{②}, \tau_{zz}^{②}\right) &= \left(\overline{h_2} + h_2', \overline{u_2} + u_2', \overline{\tau_{xx2}} + \tau_{xx2}', \overline{\tau_{zz2}} + \tau_{zz2}'\right), \\ \left(h_1, U^{①}, \tau_{xx}^{①}, \tau_{zz}^{①}\right) &= \left(\overline{h_2}\mathcal{H} + h_1', \overline{u_1} + u_1', \overline{\tau_{xx1}} + \tau_{xx1}', \overline{\tau_{zz1}} + \tau_{zz1}'\right).\end{aligned} \tag{2-45}$$

The factor $\mathcal{H}$ is a constant where it shows the relationship between the initial layers #1 and #2 heights, so $\mathcal{H} = h_1/(h_2 - h_1)$. As stated, the steady-state solution is unchanging, then the mean values are

$$\begin{aligned}\left(\overline{h_2}, \overline{u_2}, \overline{\tau_{xx2}}, \overline{\tau_{zz2}}\right) &= (0.5,\ 0,\ 0,\ 0), \\ \left(\overline{h_2}\mathcal{H}, \overline{u_1}, \overline{\tau_{xx1}}, \overline{\tau_{zz1}}\right) &= (0.5\mathcal{H},\ 0,\ 0,\ 0).\end{aligned} \tag{2-46}$$

The perturbation added in this solution follow the expressions

$$\begin{aligned}(h_2', u_2', \tau_{xx2}', \tau_{zz2}') &= (h_{02}, u_{01}, \tau_{xx01}, \tau_{zz01})\, \delta exp(\omega t + i\alpha x), \\ (h_1', u_1', \tau_{xx1}', \tau_{zz1}') &= (h_{01}, u_{02}, \tau_{xx02}, \tau_{zz02})\, \delta exp(\omega t + i\alpha x),\end{aligned} \tag{2-47}$$

where δ indicates the small amplitude of the perturbation in comparison to the variable mean value, $\delta \ll 1$. This small amplitude leads to suppression of higher order terms, i.e. $\delta^2 \to 0$. The position x is restricted to the bounded space domain $x \in \mathbb{R} / -1 < x < 1$ and the wavenumber is established as $\alpha = n\pi$, where n may take natural numbers excluding zero [14]. ω is the growth rate, which indicates how the perturbation evolves with time. The perturbation amplitude grows in case of $\omega > 0$ or reduces with time progression in case of a negative growth rate, $\omega < 0$. When $\omega = 0$, the perturbation is not affected by time. Therefore, we shall isolate the term ω to analyze how the system behaves and point out which parameters influence system stability. Proceeding, the proposed solution relations presented by Equation (2-45) are used on the viscoelastic system presented in Section 2.6. Then, the system becomes

$$
\begin{aligned}
&\frac{\partial h_1'}{\partial t} + \overline{h_2}\mathcal{H}\frac{\partial u_1}{\partial x} = 0,\\
&\frac{\partial u_1'}{\partial t} - 3S\frac{\partial^3 h_1'}{\partial x^3} - 4D\frac{\partial^2 u_1'}{\partial x^2} - E\left(\frac{\tau_{xx1}}{\partial x} - \frac{\partial \tau_{zz1}}{\partial x}\right) +\\
&\qquad\qquad + \frac{\mathbb{L}}{\overline{h_2}\mathcal{H}}\left(u_1' - u_2'\right) - \frac{3}{16}A_1\frac{1}{\left(\overline{h_2}\mathcal{H}\right)^4}\left(\frac{\partial h_1'}{\partial x}\right) = 0,\\
&\frac{\partial h_2'}{\partial t} + \overline{h_2}\frac{\partial u_2}{\partial x} = 0,\\
&\frac{\partial u_2'}{\partial t} - 3S\frac{\partial^3 h_2'}{\partial x^3} - 4\frac{\partial^2 u_2'}{\partial x^2} - L\left(\frac{\partial \tau_{xx2}'}{\partial x} - \frac{\partial \tau_{zz2}'}{\partial x}\right) - \frac{3}{16}A_2\frac{1}{\overline{h_2}^4}\left(\frac{\partial h_2'}{\partial x} - \frac{\partial h_1'}{\partial x}\right) = 0,\\
&De\frac{\partial \tau_{xx1}'}{\partial t} = -\tau_{xx1} + 2\eta_r\frac{\partial u}{\partial x},\\
&De\frac{\partial \tau_{zz1}'}{\partial t} = -\tau_{zz1} - 2\eta_r\frac{\partial u}{\partial x},\\
&De\frac{\partial \tau_{xx2}'}{\partial t} = -\tau_{xx2} + 2\eta_r\frac{\partial u}{\partial x},\\
&De\frac{\partial \tau_{zz2}'}{\partial t} = -\tau_{zz2} - 2\eta_r\frac{\partial u}{\partial x}.
\end{aligned}
\tag{2-48}
$$

Using the relations presented in the Equations (2-46) and (2-47) in the system (2-48) we get

$$
\begin{aligned}
&\omega^2 + \frac{3S}{2}\left(1+\mathcal{H}\right)\alpha^4 + 4D\alpha\omega + \frac{4E\eta_r\alpha^2\omega}{1+De\omega} + \frac{2L}{\mathcal{H}}\frac{u_{01}-u_{02}}{u_{01}}\omega - 6\frac{A_1}{\mathcal{H}^3}\alpha^2 = 0,\\
&\omega^2 + \frac{3S}{2}\left(1+\mathcal{H}\right)\alpha^4 + 4\alpha\omega + \frac{4L\eta_r\alpha^2\omega}{1+De\omega} - 6A_2\alpha^2 = 0.
\end{aligned}
\tag{2-49}
$$

Those relations are related to the first and second layers, respectively. From them, as the system is stable for $\omega <= 0$, the stability criteria shows that the first layer of the curtain is stable when

$$
\frac{S}{A_1} >= \frac{4}{\pi^2\left(1+\mathcal{H}\right)\mathcal{H}^3}, \tag{2-50}
$$

and the second layer is stable when

$$
\frac{S}{A_2} >= \frac{4}{\pi^2\left(1+\mathcal{H}\right)}. \tag{2-51}
$$

Considering the stability criteria relations in Equations (2-50) and (2-51), it is plotted in Figure 2.11 a chart to graphically analyze the proposal behavior. It is also relevant to notice that the equations are coupled. So, the evolution of one layer disturbs how the other grows. Equivalent ratios will be adopted in our simulations to avoid further complications.

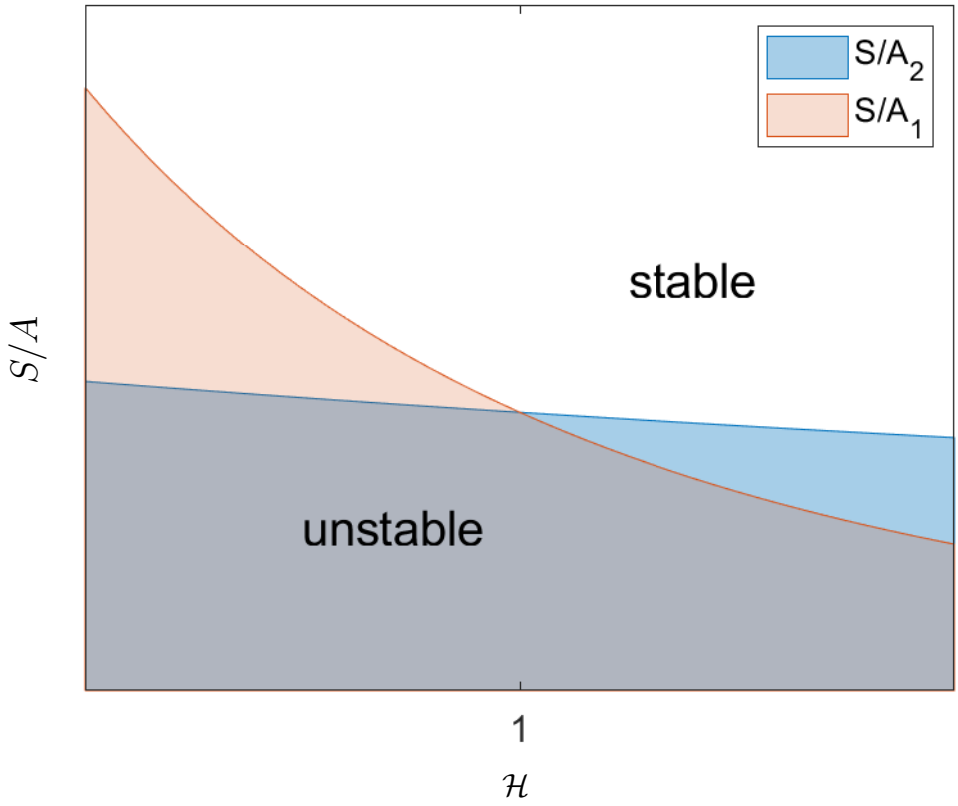

Figure 2.11: Sketch of the designed system stability map. The colored area indicates an unstable region. Vertical axis indicates the S/A ratio. For $\mathcal{H} < 1$, the second layer of fluid, in red, keeps stable longer than the first layer fluid, in blue, in a decrease of S/A. The opposite is true for $\mathcal{H} > 1$ values.

3
Solution Method

This Chapter discusses the numerical method used to solve the set of equations describing sheet evolution reported in the previous Chapter. The partial differential equations were discretized using first and second-order finite difference approximation. Also, the time discretization of the derivatives applied an implicit Crank-Nicolson method, so we avoid solution oscillations. Finally, Newton's iterative method is applied to solve the non linear system of algebraic equations at each time step.

3.1
The Finite Difference Method

The calculus of finite differences is the foundation of the Finite Difference Method (FDM). This method provides a numerical solution of simple implementation to partial differential equations (PDEs). The finite difference calculus is derived from Taylor series expansions and approximates a derivative of a given PDE. It is a relatively straightforward method in which the governing PDE is satisfied at a set of prescribed interconnected points within the computational domain, referred to as nodes [31]. The framework of connected nodes is known as a mesh. Then, each derivative on a PDE is approximated through finite differences in all nodes on the grid. Succeeding, the approximated values are substituted on the equation.

Following the works [19, 30], this work presents a unidimensional staggered grid, meaning that the problem variables are computed in different spots. The nodes associated with the u and τ variables are placed in the middle of h related nodes. Figure 3.1 shows how this grid is assembled. This kind of grid is adopted, so we have a strong coupling between the alternating variables, which avoids some types of convergence problems [32]. It also reduces the distance of adjacent nodes and avoids interpolation when calculating other variable derivatives. Then, it is possible to achieve a relative increase in result accuracy and avoid some spurious results in the long time limit. The mesh covers the $0 \leq x \leq L$ interval, which comprehends from the section where the minimum cross-sectional area is placed to the end of the oscillation, as presented in Figure 3.1. We define nodes position using the MATLAB function

logscale, which returns a vector containing a logarithmic scale starting at a given initial point and ending at an established final point. The length of this vector is also set in the function input. The goal of this procedure is to have a more refined mesh (shorter distance between the nodes) in regions where the variable gradients are higher.

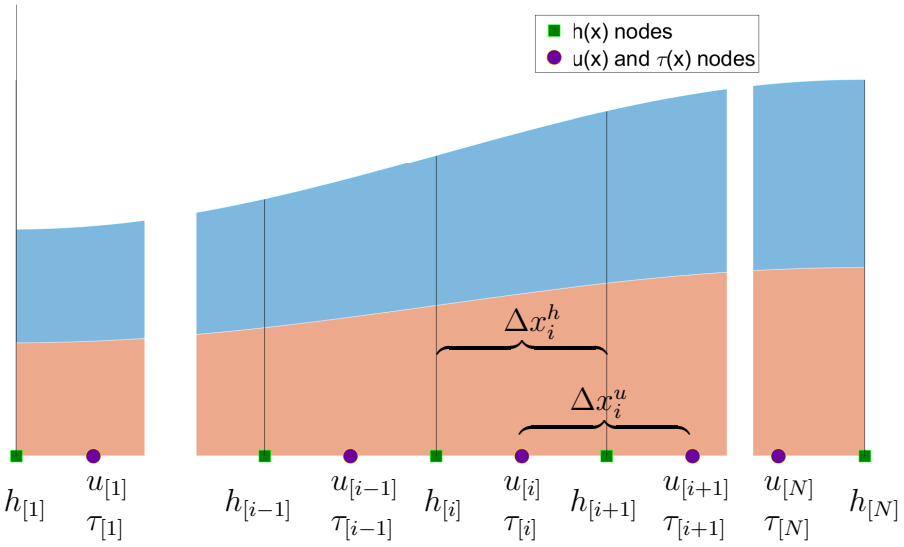

Figure 3.1: Sketch representing the unidimensional staggered grid. The u and τ nodes, in purple, and the h nodes, in green, alternate between themselves intermittently. This grid enables problem discretization and, consequently, to solve the PDEs related to the system evolution.

A central finite difference scheme (CDS) is used to approximate the derivative operators. The CDS is one of the possible results of a truncated Taylor series discretization to approximate derivatives. A Taylor series truncated after the first term approximates the desired derivative. The discretization in a CDS accounts for the forward and backward nodes from the reference node, as it is explored next in Equations (3-2) and (3-3). Firstly, we define the distances between the nodes, which are used on the derivative calculations. These distances are

$$\begin{aligned} \Delta x_i^h &= x_{i+1}^h - x_i^h, \ \textit{and} \\ \Delta x_i^u &= x_{i+1}^u - x_i^u, \end{aligned} \tag{3-1}$$

in which, x_i^h is the x coordinate value of the $h_{[i]}$ node and x_i^u is the x coordinate value of the $u_{[i]}$ node. The index i indicates the node position on the grid. The calculation of variables and derivatives on x_i points for Equations I and III, Equations (2-35) and (2-37), in the system of differential equations follow a CDS accordingly to

$$
\begin{aligned}
&h_j(x_i^h) \cong h_{j[i]},\\
&u_j(x_i^h) \cong \frac{u_{j[i]}\Delta x_i^h + u_{j[i-1]}\Delta x_{i-1}^h}{\Delta x_i^h + \Delta x_{i-1}^h},\\
&\frac{\partial h_j}{\partial x}(x_i^h) \cong \frac{h_{j[i+1]} - h_{j[i-1]}}{\Delta x_i^h + \Delta x_{i-1}^h},\\
&\frac{\partial u_j}{\partial x}(x_i^h) \cong \frac{u_{j[i]} - u_{j[i-1]}}{\Delta x_{i-1}^u},
\end{aligned}
\tag{3-2}
$$

where the j index indicates the fluid layer. On the other hand, the variables and derivatives approximation in x_i for the remaining Equations of the differential equation systems described in Section 2.6 come as

$$
\begin{aligned}
&u_j(x_i^u) \cong u_{j[i]},\\
&\tau_{xxj}(x_i^u) \cong \tau_{xxj[i]},\\
&\tau_{zzj}(x_i^u) \cong \tau_{zzj[i]},\\
&h_j(x_i^u) \cong \frac{h_{j[i]}\Delta x_{i-1}^u + h_{j[i+1]}\Delta x_i^u}{\Delta x_i^u + \Delta x_{i-1}^u},\\
&\frac{\partial u_j}{\partial x}(x_i^u) \cong \frac{u_{j[i+1]} - u_{j[i-1]}}{\Delta x_i^u + \Delta x_{i-1}^u},\\
&\frac{\partial \tau_{xxj}}{\partial x}(x_i^u) \cong \frac{\tau_{xxj[i+1]} - \tau_{xxj[i-1]}}{\Delta x_i^u + \Delta x_{i-1}^u},\\
&\frac{\partial \tau_{zzj}}{\partial x}(x_i^u) \cong \frac{\tau_{zzj[i+1]} - \tau_{zzj[i-1]}}{\Delta x_i^u + \Delta x_{i-1}^u},\\
&\frac{\partial h_j}{\partial x}(x_i^h) \cong \frac{h_{j[i+1]} - h_{j[i]}}{\Delta x_i^h},\\
&\frac{\partial^2 u_j}{\partial x^2}(x_i^u) \cong \frac{\Delta x_{i-1}^u u_{j[i+1]} - \left(\Delta x_i^u + \Delta x_{i+1}^u\right) u_{j[i]} + \Delta x_i^u u_{j[i-1]}}{\Delta x_i^u \Delta x_{i-1}^u \left(\Delta x_i^u + \Delta x_{i-1}^u\right)/2},\\
&\frac{\partial^2 h_j}{\partial x^2}(x_i^h) \cong \frac{\Delta x_{i-1}^h h_{j[i+1]} - \left(\Delta x_{i-1}^h + \Delta x_i^h\right) h_{j[i]} + \Delta x_i^h h_{j[i-1]}}{\Delta x_i^h \Delta x_{i-1}^h \left(\Delta x_i^h + \Delta x_{i-1}^h\right)/2},\\
&\frac{\partial^2 h_j}{\partial x^2}(x_i^h, x_i^u) \cong \left(x_i^u \frac{\partial^2 h_j(x_{i+1}^h)}{\partial x^2} + x_{i-1}^u \frac{\partial^2 h_j(x_i^h)}{\partial x^2}\right) / \left(\Delta x_i^u + \Delta x_{i-1}^u\right),\\
&\frac{\partial^3 h_j}{\partial x^3}(x_i^h) \cong \left(\frac{\partial^2 h_j(x_{i+1}^h)}{\partial x^2} - \frac{\partial^2 h_j(x_i^h)}{\partial x^2}\right) / \Delta x_i^h.
\end{aligned}
\tag{3-3}
$$

3.2 Crank-Nicolson method

The set of PDEs is solved as an initial value problem since we have equations that describe a system evolving in time, and we impose an initial configuration for this system in the initial time, $t = 0$. While the problem space aspect requires two boundary conditions, considering it stands presenting

characteristics of elliptical equations, the time aspect is only supplied with a single initial condition, as the equations are first order from time perspective. Therefore, it is stipulated a small time step, Δt, to numerically solve the given set of equations. The system solution in a particular time, t^n, is used as a basis to manage to solve the forward time step, $t^{n+1} = t^n + \Delta t$. The algorithm obeys this pattern until it reaches a specified time point. Then the solution across the desired time range is reached.

To solve the system, for the forward time step calculation, it is used as an approximation of the calculus' mean value theorem. The theorem states that given a continuous function, $f(t)$, in a domain range, Δt, the derivative of at least one point in this range, $t = t_{spot}$, equals the derivative of the linear function passing through the outer points from this range. Mathematically,

$$\frac{\partial f(t_{spot})}{\partial t} = \frac{f(t + \Delta t) - f(t)}{\Delta t}. \tag{3-4}$$

We rewrite the term $f(t + \Delta t) - f(t)$ using a notation that indicates the variable manipulation on the discrete time grid, $f^{n+1} - f^n$. As we cannot determine which is the t_{spot} point, the Crank-Nicolson method approximates it. This method uses two common approximations of t_{spot} and combines them. The first approximation is the one used in the explicit method, where $t_{spot} = t^n$. The remaining approximation is from an implicit method, where $t_{spot} = t^{n+1}$. Those approximations do not deviate much from the actual t_{spot} value because the considered range Δt is considerably small. The Crank-Nicolson method is a straight line interpolation between the results from these both estimates, which is called the trapezoid rule [32]. Considering that, the above expression becomes [31]

$$f^{n+1} = \frac{\alpha}{2}\left(\frac{\partial f^{n+1}}{\partial t} + \frac{\partial f^n}{\partial t}\right)\Delta t + f^n. \tag{3-5}$$

$\partial f^{n+1}/\partial t$ and $\partial f^n/\partial t$ are computed from function values in the spatial grid points using Section 2.6 equations and the discretization showed in Equations (3-2) and (3-3). Since the computation of the variable we intend to calculate, f^{n+1}, requires the employment of this same variable, this method is defined as implicit. The usage of implicit methods is valuable, as they offer improved stability, which allows solving stiff equations using larger time steps than it is necessary to solve them in explicit methods.

3.3 Newton's method

After spacial and time discretization, we obtain a non-linear set of algebraic equations at each time step that describes the nodal values at t^{n+1}.

Newton's method is the solver adopted among a range of non-linear equation solving techniques. An intrinsic advantage of the method is its convergence speed. Differently, its negative aspect is the Jacobian computation requirement, which is very costly for large equations.

Newton's method uses the first two terms of Taylor series expansion to linearize the set of equations, $\boldsymbol{f}(\boldsymbol{x})$, and then find its roots. Demonstrating the Taylor linearization in a single equation, the process to find the root would isolate x in the expression $f(x) \cong f(x_0) + (\partial f(x_0)/\partial x)\,(x - x_0) = 0$. Then, for a system of n equations we have

$$f_i(\boldsymbol{x}) \cong f_i(\boldsymbol{x}^k) + \left(\boldsymbol{x}^{k+1} - \boldsymbol{x}^k\right) \frac{\partial f_i(\boldsymbol{x})}{\partial x_j} = 0, \tag{3-6}$$

for $i = 1, \ldots, n$, $j = 1, \ldots, n$, $\boldsymbol{x}$ is the root vector of n elements, and k is the iteration index. The matrix $\partial f_i(\boldsymbol{x})/\partial x_j$ is known as Jacobian and is represented as J_{ij}. So, the root is easily found following

$$\begin{aligned} \left(\boldsymbol{x}^{k+1} - \boldsymbol{x}^k\right) &= -J_{ij}^{-1} f_i(\boldsymbol{x}^k), \\ \boldsymbol{x}^{k+1} &= \boldsymbol{x}^k + \left(\boldsymbol{x}^{k+1} - \boldsymbol{x}^k\right). \end{aligned} \tag{3-7}$$

The method converges quadratically when the first estimate is near the system root. I.e. the error at iteration $k + 1$ is proportional to the square of the error at iteration k [32]. Then, it needs only a few iterations to reach a solution once the system estimate gets close to the root.

4
Results

This chapter presents the results of the analysis. First, the model derivation and implementation is validated by comparing the predictions considering both layers of the same liquid with results presented in the literature for single layer liquid sheets. Then, the results for the two-layer systems are presented and discussed.

4.1
Validation

The model validation was conducted by comparing the predictions obtained for a single layer sheet with results presented in the literature. The time evolution of the liquid sheet was compared with the results presented by Bazzi et al. [19]. As previous works studied the evolution of single-layer sheets, the validation was performed using the same fluid parameters for both layers. This validation examines the temporal thickness evolution and compares the behavior to the reference works. The evaluation was performed for Newtonian, GNM, and Oldroyd-B models. Hence, the proposed model must show similar sheet surface progress to be considered correctly implemented. The rupture times predicted by the proposed models and the values reported by Bazzi et al. [19, 33] are also compared. The initial sheet profile for validation is as described in Section 2.7. The final rupture time is taken when the minimum sheet height is less than 20% of the initial sheet's height mean value. Figure 4.1 shows the sheet surface profile for a Newtonian sheet in the instant when rupture occurrence is considered. Similarly, Figure 4.2 considers the rupture sheet profile for a Oldroyd-B viscoelastic liquid with $\eta_r = 8$ and $De = 0.5$. The proposed model recovers the literature final sheet profile in both cases. Considering the evolution of the minimum thickness with time, Figure 4.3 shows that the evolution presented in the literature and obtained with the proposed model for Newtonian sheets are similar. Likewise, Figure 4.4 exhibits that the Oldroyd-B proposed model also recovers literature behavior concerning the perturbation evolution. Regarding the models in broad circumstances, Figures 4.5 and 4.6 compare the proposed models and [19] models rupture times for different fluid parameters. Figure 4.5 compares the Oldroyd-B model

rupture times for multiple η_r and De values. As these values increase, the non-Newtonian fluid characteristic gets stronger. It is perceptible that fluids with a stronger non-Newtonian nature have a further delay in rupture time. Figure 4.6 compares rupture times for GNM models and has similar behavior, the increase in non-Newtonian characteristics leads to extended times to sheet breakup.

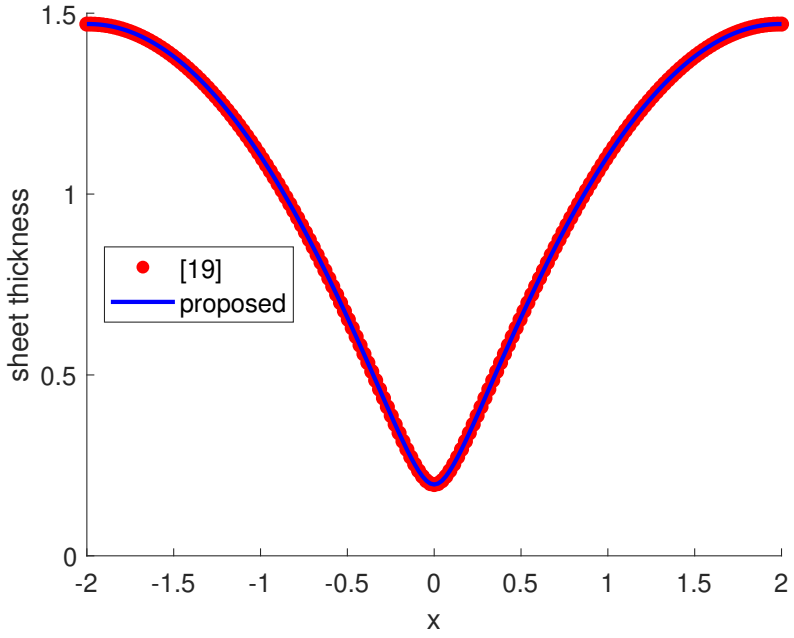

Figure 4.1: Graphical comparison of sheet profile at the rupture instant between the [19] Newtonian model and the proposed Newtonian model. The proposal recovers the literature final sheet profile.

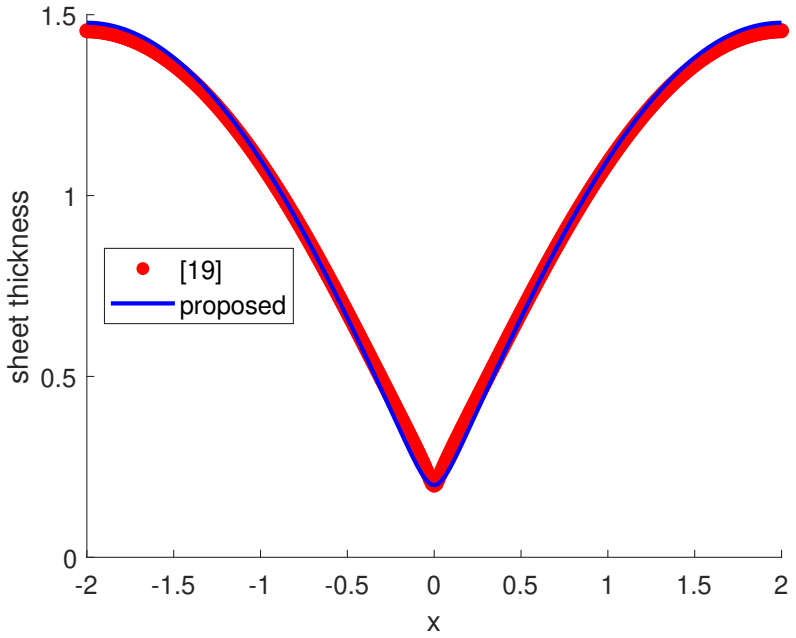

Figure 4.2: Graphical comparison of sheet profile at the rupture instant between the [19] Oldroyd-B model and the proposed Oldroyd-B model, where the fluid parameters are $\eta_r = 8$ and $De = 0.5$. The proposal recovers the literature final sheet profile.

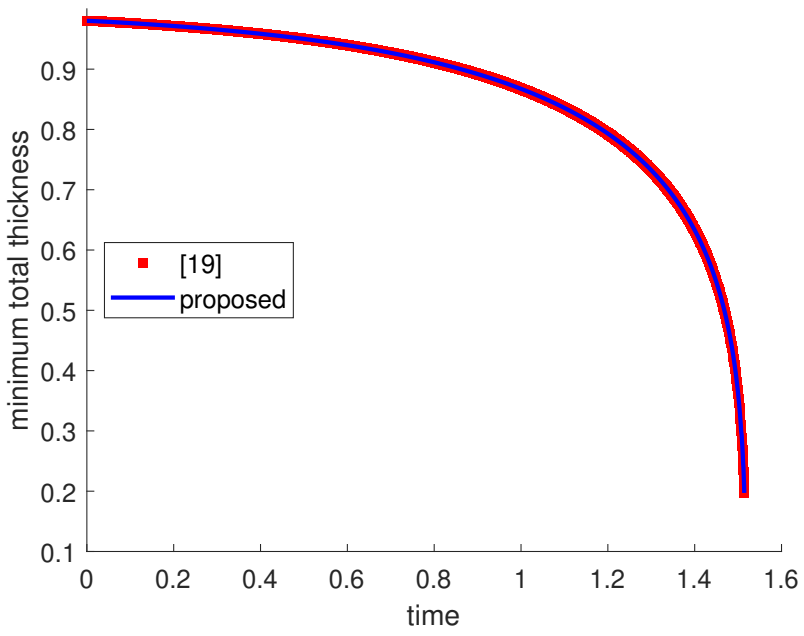

Figure 4.3: Graphical comparison of minimum total thickness in the sheet profile over time between the [19] Newtonian model and the proposed Newtonian model. The proposal recovers the behavior described in the literature for the perturbation evolution.

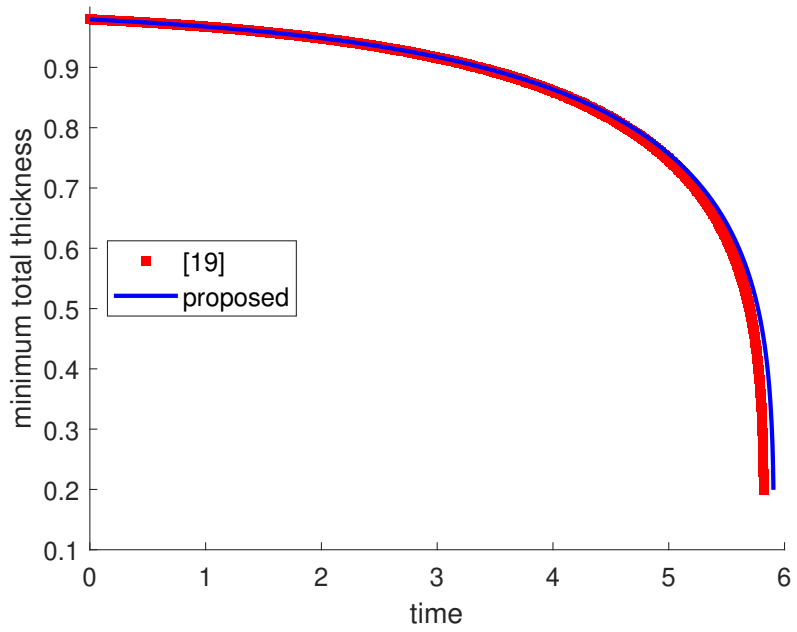

Figure 4.4: Graphical comparison of minimum total thickness in the sheet profile over time between the [19] Oldroyd-B model and the proposed Oldroyd-B model, where the fluid parameters are $\eta_r = 8$ and $De = 0.5$. The proposal recovers the behavior described in the literature for the perturbation evolution.

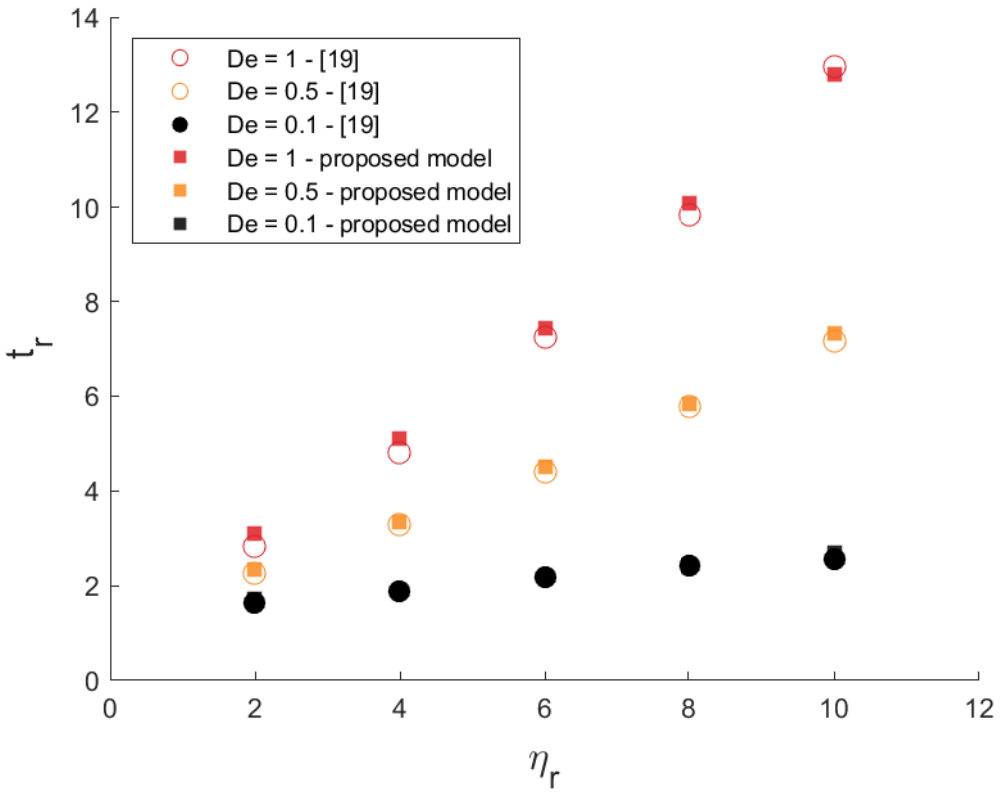

Figure 4.5: Graphical comparison of rupture times between the [19] Oldroyd model and the proposed Oldroyd model. The proposal recovers the literature rupture times effectively.

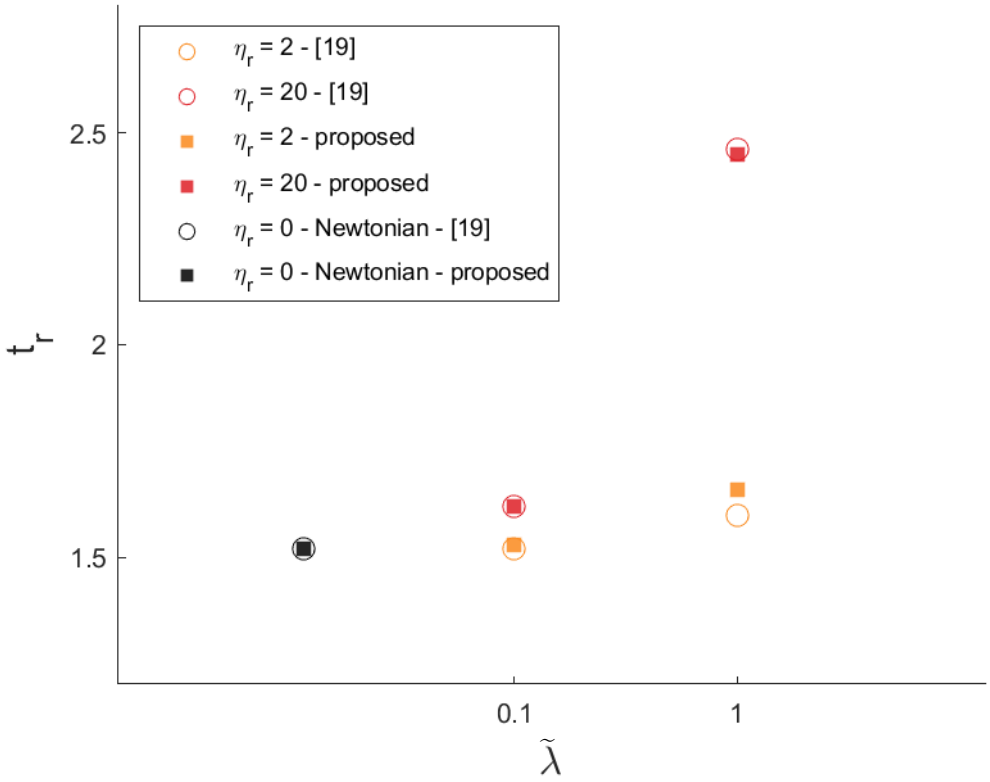

Figure 4.6: Graphical comparison of rupture times between the [19, 33] GNM and Newtonian models and the proposed models. The proposal recovers the presented rupture times published.

4.2 Single layered sheets

The validation was performed using the two-layer model to simulate a single-layer sheet. This enables detail analysis of some conclusions of previous works. The validation data presented provide enough information to notice the effects of non-Newtonian physics on rupture times of single-layered sheets. Figure 4.5 shows that as the non-Newtonian characteristic in a fluid become more intense, characterized by higher Deborah number for the Oldroyd-B model, De, or Carreau number for the Generalized Newtonian model, $\tilde{\lambda}$, and relative viscosities, η_r, the rupture instant is further delayed. It comes from the tension-thickening nature of the fluids. Figure 4.7 exhibits the intensity of different forces along the sheets in a near rupture moment. It is noticeable that the van der Waals forces are in opposite direction to all other forces, which is expected since van der Waals are the only driving force for the pertubation growth and all other forces resist the flow. Capillary and van der Waals forces define the stability of the curtain, while viscous related forces affect the rupture

time. Therefore, the viscoelastic force delays the sheet breakup. Lastly, the interfacial force, which comes from the tangential forces between the layers, Equation (2-19), remain null in this single layer situation. As both layers have the same properties, that is the expected since tangential forces between the two layers is only present if they have different viscosities.

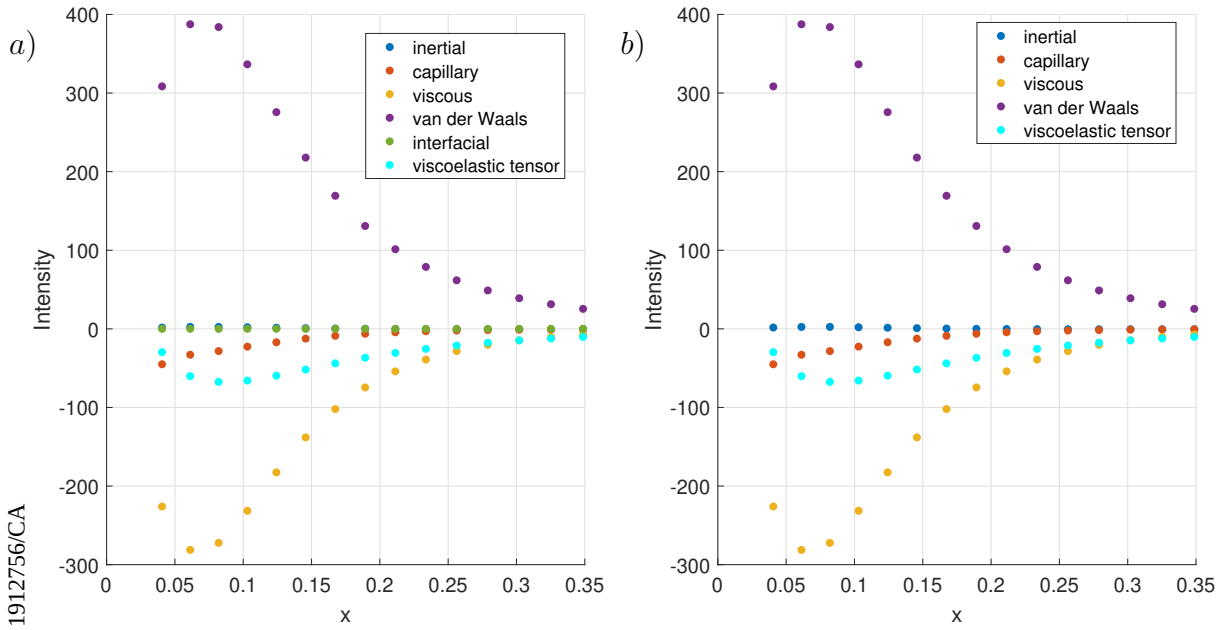

Figure 4.7: Individual forces in the initial 15% of the domain. Both layers are represented on the instant about to occur sheet breakup. It is a simulation of a single-layered sheet. Both viscoelastic layers have the fluid properties $\eta_r = 4$ and $De = 0.5$. a) Forces intensity in the sheet's first layer. b) Forces intensity in the sheet's second layer.

The solutions provided by the single-layer sheet simulations enable us to study how the linear stability analysis impacts the final answer. Then, we consider sets of single-layered sheets. These sheets are composed of two layers of the same fluid, so we vary the thickness ratio, $\mathcal{H}$, to show that the developed stability analysis relationship provides equal conditions despite changes in $\mathcal{H}$. The S/A ratio in the layers are given by the constant γ, defined as:

$$\gamma = \frac{S/A}{S/A_{cr}}, \tag{4-1}$$

where S/A_{cr} is the critical value of S/A ratio, given by Equations (2-50) and (2-51). Then, S/A ratio is computed by

$$\begin{aligned} \frac{S}{A_1} &= \frac{4\gamma_1}{\pi^2\,(1+\mathcal{H})\,\mathcal{H}^3}, \\ \frac{S}{A_2} &= \frac{4\gamma_2}{\pi^2\,(1+\mathcal{H})}. \end{aligned} \tag{4-2}$$

In this work we simulate the curtains in which both layers have the same values of γ, meaning that $\gamma = \gamma_1 = \gamma_2$. Rupture times of unstable sheets, $\gamma < 1$, are displayed in Table 4.1.

From the Table 4.1 data, it is perceptible that when γ is constant, the change in $\mathcal{H}$ will not alter rupture time. So, the developed stability analysis generates equal initial conditions, regarding the proportion of capillary and surface tension forces, at thickness ratio change when the constant γ remains unchanged in Equation (4-2). This result was expected. When the properties of both layers are equal, the thickness ratio should not affect the solution and the sheet behaves as a single layer film.

		γ		
		1/4	2/4	3/4
$\mathcal{H}$	0.8	1.954	2.827	5.199
	0.9	1.954	2.827	5.199
	1	1.954	2.826	5.198
	1.2	1.954	2.827	5.199

Table 4.1: Rupture time for a single-layered viscoelastic sheet with properties $\eta_r = 3$ and $De = 0.5$. It is varied the thickness ratio of the layers, $\mathcal{H}$. It is also varied the layers' S/A ratio by multiplying a factor, γ, to the stability threshold established.

Figure 4.8 shows whether the curtain is stable or not over a range of γ. Stability may be inferred through the analysis of the change in perturbation amplitude. The Figure shows the perturbation amplitude change from $t = 0$ to $t = 0.5$. Change in perturbation amplitude is computed as $\Delta\epsilon = \epsilon\,(t = 0.5) - \epsilon_0$ since ϵ is the deviation from the the mean profile thickness. Stability occurs when $\gamma > 1$ since this is the range at which $\Delta\epsilon < 0$, meaning that the amplitude of the perturbation is decreasing. Analogously, the curtain is unstable for $\gamma < 1$. It is also noticeable, as reported in [19], that as viscoelastic effects become stronger, the change in amplitude decreases indicating the viscoelastic forces slow down the flow. The results show that viscoelastic effects affect the flow velocity, but do not interfere with the stability criteria.

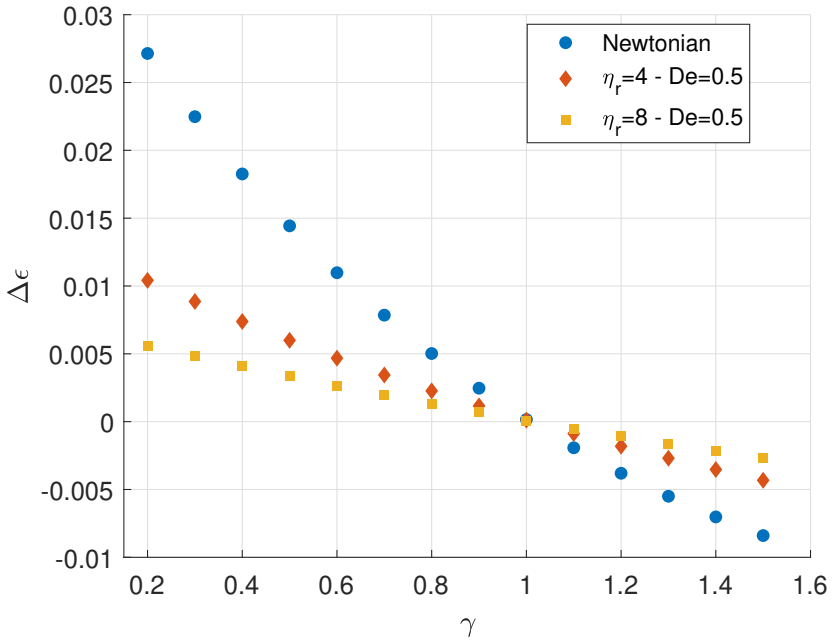

Figure 4.8: Change in perturbation amplitude over a range of γ from $t = 0$ to $t = 0.5$. $\Delta\epsilon$ is computed as $\Delta\epsilon = \epsilon\,(t = 0.5) - \epsilon_0$. Curtain is stable when $\Delta\epsilon < 0$, and unstable when $\Delta\epsilon > 0$.

4.3 Double layered sheets

In this section, we discuss the model results for curtains constituted by two layers with different fluid properties. Subsection 4.3.2 addresses sheet surface evolution. Subsection 4.3.1 discusses the rupture times. Subsection 4.3.3 examine the force distribution in the layers.

4.3.1 Sheet surface evolution

We investigate curtains constituted by two layers with different fluid properties and analyze the curtain time evolution. We also vary layer thickness ratio to obtain a broader perspective on the subject.

First, we analyze sheets constituted by two layers of Newtonian fluids. The fluid density is the same in both layers. The second layer viscosity is fixed as $\mu_2 = 1$ mPa.s, and for the first layer, viscosity, μ_1, is a factor multiplied by the viscosity μ_2. The non-dimensional thicknesses are initialized using the relationship $\mathcal{H}$ that defines the ratio between the first and second layer thickness at the initial time, $\mathcal{H} = h_1/(h_2 - h_1)$. h_1 is the height of the interface between both layers and h_2 is the total sheet height. So, they are initialized as $h_1 = 0.5\mathcal{H}$ and $h_2 = 0.5\,(1 + \mathcal{H})$. The ratio between the non-dimensionals of capillary and van der Waals forces are set according to

$S_1/A_1 = 2/\left(\pi^2\left(1+\mathcal{H}\right)\mathcal{H}^3\right)$ and $S_2/A_2 = 2/\left(\pi^2\left(1+\mathcal{H}\right)\right)$. As $\gamma = 0.5$ for those S/A ratio values, the simulated sheets are expected to be unstable. We consider as the final rupture time when the minimum sheet height is less than 20% of the initial sheet's height mean value. The actual rupture time is imminent from this final point since the rate of reduction in sheet thickness is already considerably steep when the minimum sheet height gets to this value.

Here it is considered the surface evolution of double and single-layered sheets. As the sheets are initialized with different non-dimensional thickness ratios, $\mathcal{H}$, it is performed a normalization before the sheet profile analysis.

$$\begin{aligned} h_{1norm} &= h_1/\left(0.5\left(1+\mathcal{H}\right)\right), \\ h_{2norm} &= h_2/\left(0.5\left(1+\mathcal{H}\right)\right). \end{aligned} \tag{4-3}$$

This normalization aids to perform comparisons among different conditions since the normalized upper layer always starts at the height of $1-\epsilon_0$. Figures 4.9 and 4.10 present the evolution of the normalized values of minimum height with time considering the perturbation profile of a two-layer sheet and a single-layer sheet. The former is constituted by a Newtonian and a non-Newtonian layer, while the latter is formed only by the Newtonian liquid layer. The Newtonian fluid viscosity is $\mu = 1$ mPa.s. It is shown a combination of Newtonian and GNM layers and Newtonian and Oldroyd-B layers, respectively. The GNM fluid properties are $\eta_r = 20$ and $\widetilde{\lambda} = 1$, while the Oldroyd-B fluid properties are $\eta_r = 4$ and $De = 0.5$. These Figures show that the thin non-Newtonian layer stabilizes the sheet and extends the demanded time to rupture. Figure 4.9 reveals that the decrease in thickness with time for the Newtonian single-layer sheet has a lower magnitude at the beginning of the evolution and increases rapidly during a later stage of the perturbation evolution. Conversely, the sheet with a thin layer of a GNM fluid does not significantly accelerate the thickness reduction with time. This explains the noticed increase in breakup time. On the other hand, Figure 4.10 displays for the sheet with a thin Oldroyd-B layer a behavior similar to the described to the Newtonian single-layer sheet. The rate of thickness reduction with time has a steep increase near rupture. In this case, it is inferred that the delay in breakup time is an overall reduction in the thickness reduction rate. Comparing the total thickness for these sheets over time. The sheet with the GNM layer starts the evolution with a thickness reduction rate equal to the one in the Newtonian sheet, while the sheet with the Oldroyd-B layer has a lower thickness reduction rate. The rest of the evolution is as described.

Figure 4.11 compares the profile evolution for double-layered sheets constituted by a thick Newtonian layer and a thin viscoelastic layer. It is

shown the evolution of sheets with the same fluid properties but with different thickness ratios, $\mathcal{H} = 0.15$ and $\mathcal{H} = 0.3$. It is visible that the change in thickness ratio did not modify the upper layer minimum thickness evolution.

In a comparison between the evolution of the layers' thicknesses of a Newtonian–Oldroyd-B sheet with time, it is possible to evaluate how the relationship between the layers affects the dynamics. This comparison is performed using the ratio between the layers' height percentages of its initial height. The percentages are given by

$$\begin{aligned} h_{1perc}(t) &= h_1(t) / (0.5\mathcal{H}), \\ h_{2perc}(t) &= h_2(t) / (0.5(1+\mathcal{H})). \end{aligned} \tag{4-4}$$

The ratio is calculated as

$$h_{ratio} = h_{1perc}/h_{2perc}. \tag{4-5}$$

The calculated ratio remains throughout the entire time range as $h_{ratio} \to 1$. This implies that, in the simulated conditions, both layers' rate of thickness reduction is the same. Then, for double sheets in an instability case, in which the fluid surface tension and the Hamaker constant are about the same, both layers will have their rupture together.

The reported ratio maintenance hints that the velocity profile is kept equivalent in the time domain. Figures 4.12 and 4.13 show the velocity along the sheet in the last time step for a Newtonian–Newtonian sheet, $\mu_1 = 5$ mPa.s, and a Newtonian–viscoelastic sheet, $\eta_r = 4$ and $De = 0.5$. In both cases, the modulus of the velocity profile difference goes to zero when compared to the velocity, $\mathcal{O}(-3)$ and $\mathcal{O}(1)$ respectively, which confirms the previous hypothesis. Although the difference between velocity profiles in the different layers is small, it is enough to produce high shear stress values. Shear stress and the other forces are discussed in detail in Subsection 4.3.3.

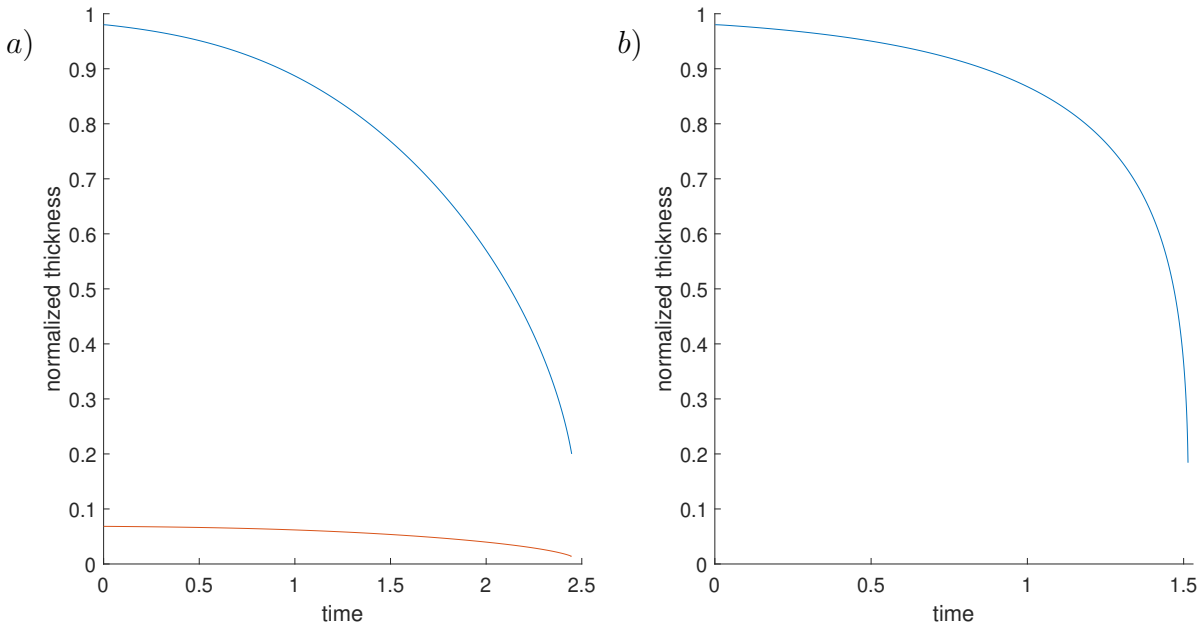

Figure 4.9: Normalized minimum thickness over time. a) A sheet constituted by a thick Newtonian layer and a thin GNM layer with the fluid properties $\eta_r = 20$, $\tilde{\lambda} = 1$, and $\mathcal{H} = 0.2$. b) A single sheet of Newtonian fluid, $\mu = 1$ mPa.s.

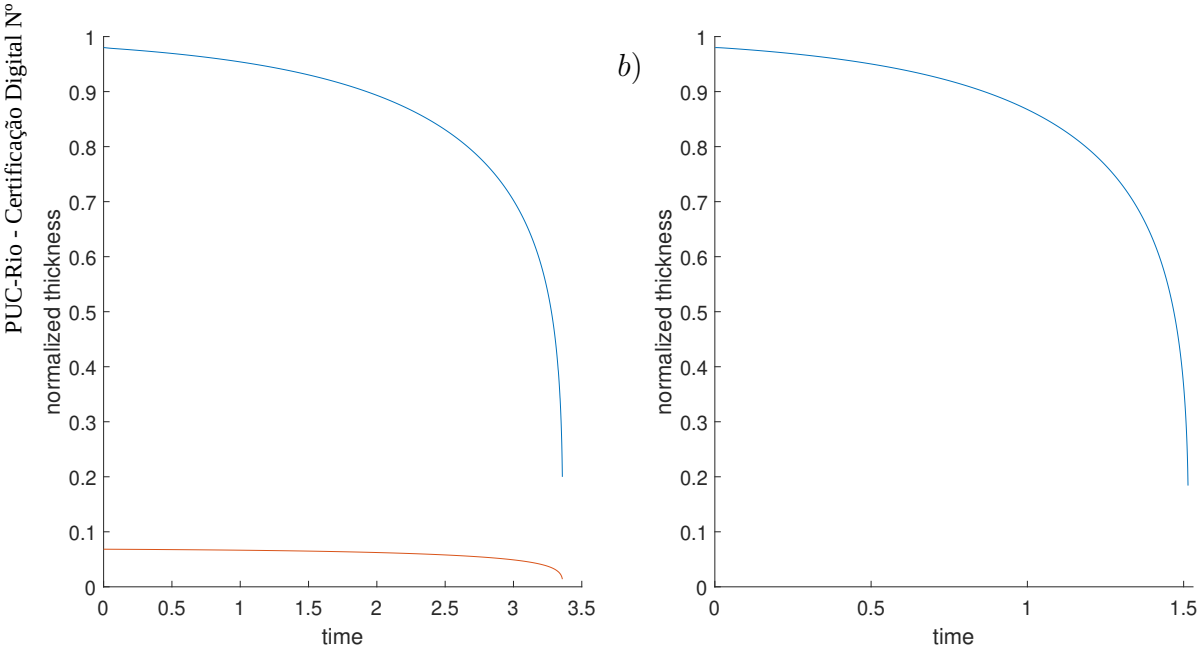

Figure 4.10: Normalized minimum thickness over time. a) A sheet constituted by a thick Newtonian layer and a thin viscoelastic layer with the fluid properties $\eta_r = 4$, $De = 0.5$, and $\mathcal{H} = 0.15$. b) A single sheet of Newtonian fluid, $\mu = 1$ mPa.s.

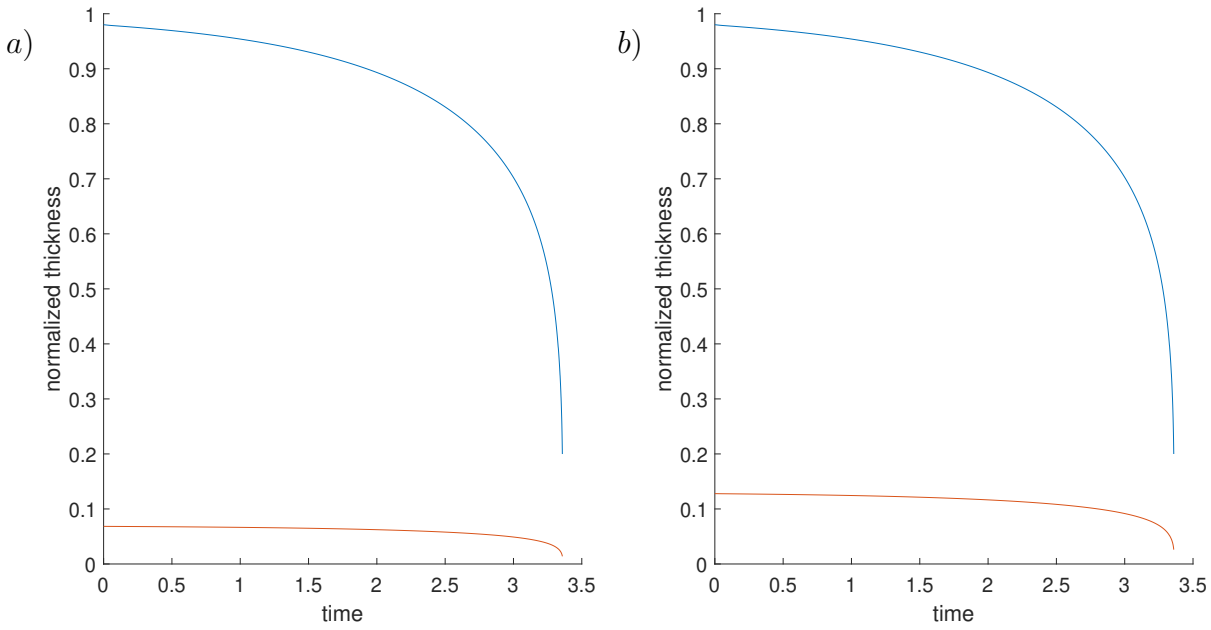

Figure 4.11: Normalized minimum thickness over time. a) A sheet constituted by a thick Newtonian layer and a thin viscoelastic layer with the fluid properties $\eta_r = 4$, $De = 0.5$, and $\mathcal{H} = 0.15$. b) It is changed the parameter $\mathcal{H} = 0.3$.

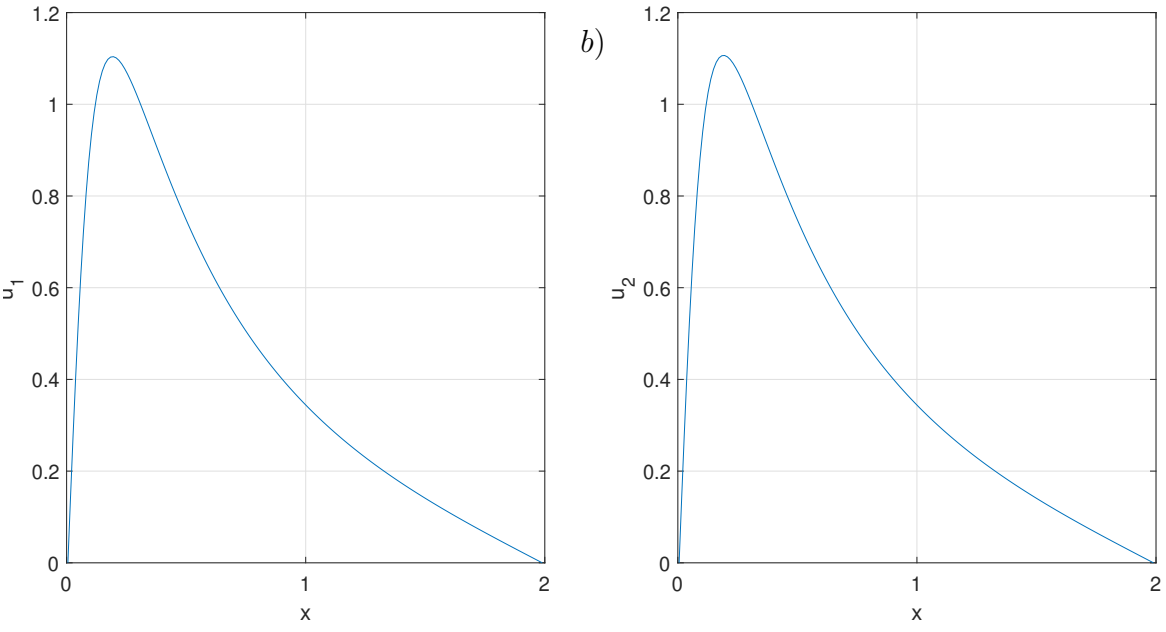

Figure 4.12: Velocity profile in the entire sheet length when the sheet is about to pinch-off. Both layers are Newtonian. a) Velocity profile in the sheet's first layer with fluid property $\mu_1 = 5$ mPa.s. b) Velocity profile in the sheet's second layer with fluid property $\mu_2 = 2$ mPa.s.

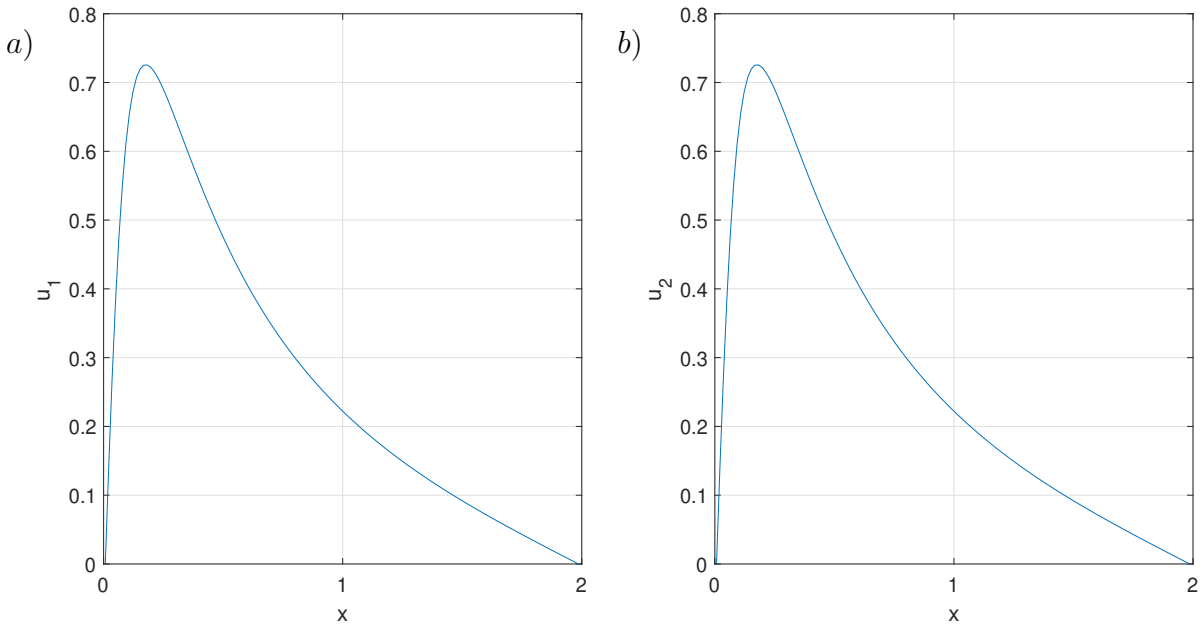

Figure 4.13: Velocity profile in the entire sheet length when the sheet is about to pinch-off. The sheet is constituted by a Newtonian layer and a viscoelastic layer with the fluid properties $\eta_r = 4$, $De = 0.5$, and $\mathcal{H} = 0.15$. a) Velocity profile in the sheet's first layer. b) Velocity profile in the sheet's second layer.

4.3.2 Rupture time

The rupture time of different sheets are considered in this subsection. For the Newtonian–Newtonian sheets, the dimensionless rupture time does not exhibit large variation with the viscosity ratio and thickness ratio, as shown in Table 4.2. So, independently of the viscosity ratio among the fluids or layer thickness ratio, the non-dimensional times until the pinch-off were about the same. This numerical result obtained agrees with experimental data [18]. Experimental measurements [18] have shown that by substituting the fluid of one layer for another fluid with 3.3 times its viscosity, the critical flow rate for curtain breakup remains within the same range. The flow rate examined in [18] is related to the breakup time computed since the flow rate determines the dimensional sheet thickness. Also, the necessary time to occur the burst in the curtain depends on the experimental set configuration. The longer the falling height is, the longer the perturbation will have to stay on the sheet. So, in a breakup case, the maximum time to rupture in an experimental set is fixed.

		μ_1 [mPa.s]		
		2	5	10
$\mathcal{H}$	0.3	1.519	1.518	1.516
	0.4	1.519	1.518	1.514
	0.6	1.517	1.516	1.508

Table 4.2: Rupture time for Newtonian–Newtonian sheets. It is displayed for different values of viscosity in the sheet's first layer, μ_1. It is also varied the thickness ratio of the layers, $\mathcal{H}$. The rupture time for a single layer sheet of Newtonian fluid is $t_r = 1.52$.

Subsequently, it comes the analysis of sheets constituted by a Newtonian and non-Newtonian layers. As in the previous case, we have both layers with the same density. The viscosity of the Newtonian layer is $\mu = 1$ mPa.s, while the non-Newtonian layer follows either a GNM model or a Oldroyd-B model. The GNM is set with the parameters $\eta_r = 20$ and $\widetilde{\lambda} = 1$, while the Oldroyd-B model is set with $\eta_r = 4$ and $De = 0.5$. The initial non-dimensional layers' thicknesses and the ratio S/A are set just as described in the previous Subsection.

The Newtonian–non-Newtonian sheets results for rupture time are listed in Table 4.3. Comparing these values with the ones presented in Table 4.3, we can notice that the system rupture time of a two-layer sheet with a thin viscoelastic layer takes longer to pinch-off than a single sheet Newtonian layer. This explains the results presented by Karim et al. in [13], which experimentally showed a drastic reduction on minimum sheet thickness for stable curtains by using a viscoelastic thin layer as one of the layers of a two-layer sheet. They measured the reduction in minimum sheet thickness when a shear-thinning fluid sheet was substituted by a double layer sheet constituted of the previous fluid and a thin layer of a viscoelastic liquid. So, the viscoelastic layer improved stability and has allowed reducing the minimum thickness of a sheet that had to be thicker to remain stable. The results presented here support this experimental finding. Moreover, according to the results presented in Table 4.3 and Figure 4.11, at least until the explored thickness ratio, the thickness ratio do not significantly change the sheet rupture time. Therefore, maintaining the total dimensional sheet thickness, the proportion between the sheet layers thickness can be freely altered to fit a given application, rupture time will remain constant.

$\mathcal{H}$	GNM	Oldroyd-B
0.15	2.4477	3.3590
0.2	2.4474	3.3585
0.3	2.4472	3.3578

Table 4.3: Rupture time for Newtonian–non-Newtonian sheets. The Newtonian layer viscosity is $\mu = 1$ mPa.s. For the non-Newtonian layer we have a GNM model with $\eta_r = 20$ and $\widetilde{\lambda} = 1$, and a Oldroyd-B model with $\eta_r = 4$ and $De = 0.5$. The rupture time for a single layer GNM sheet with the given fluid properties is $t_r = 2.446$, while the single-layer Oldroyd-B sheet has the rupture time $t_r = 3.36$. It is varied the thickness ratio of the layers, $\mathcal{H}$, in a way that the non-Newtonian layer is the thinner one.

4.3.3 Force distribution

The analysis of force distribution on the layers allows better understading of the phenomena reported in the previous subsections. Figure 4.14 shows the sum of forces in a Newtonian–viscoelastic double-layer sheet. It is apparent that the sum of forces in one layer is analogous to the sum of forces in the other one. This justifies the equivalent velocity profiles found in Figures 4.12 and 4.13, which generates the sheet surface profile evolution perceived. As both layers undergo the same resultant force intensity, the pairing velocity evolution related in the previous section is explained.

Figure 4.15 shows the individual forces intensity that act on the sheet along its length. We can see in the right plot viscoelastic layer forces. Besides the null inertial forces, there are capillary forces, viscous forces, van der Waals forces, and the Oldroyd-B viscoelastic forces. The van der Waals forces are opposite in direction from all other forces, so it is the only force acting towards rupture. In the left plot, it is described the forces acting on the Newtonian layer. In addition to the inertial forces, the viscoelastic forces are also null since it is a Newtonian liquid model. The capillary and van der Waals cannot be perceived in the plot due to the thickness ratio, which provoked its modulus reduction. The viscous force magnitude does not alter or get influenced by the thickness ratio. The interfacial forces modulus, from Equation (2-19), is remarkable. The interfacial forces rise substantially according to sheet thickness ratio and fluid parameters difference in the different layers, although the velocity profile difference between the layers is visually undetectable, as shown in Figures 4.12 and 4.13, and the interfacial forces are computed from the layers' difference in velocity profile, this difference is enough to produce the effect of generating a force of large modulus. For the Newtonian layer, in Figure 4.15, the interfacial forces are the greatest in magnitude. So, the interfacial forces lead to the

equivalent sum of forces in the layers observed in Figure 4.14, and their outcomes. The interfacial forces are only present in the Newtonian layer chart because the system is only evaluated at the interfacial surface height, h_1, and at the total sheet thickness height, h_2. As shear stress in h_2 is null due to the free surface boundary condition, Equation (2-16), there is no direct interfacial force effect for the viscoelastic layer in the proposed system.

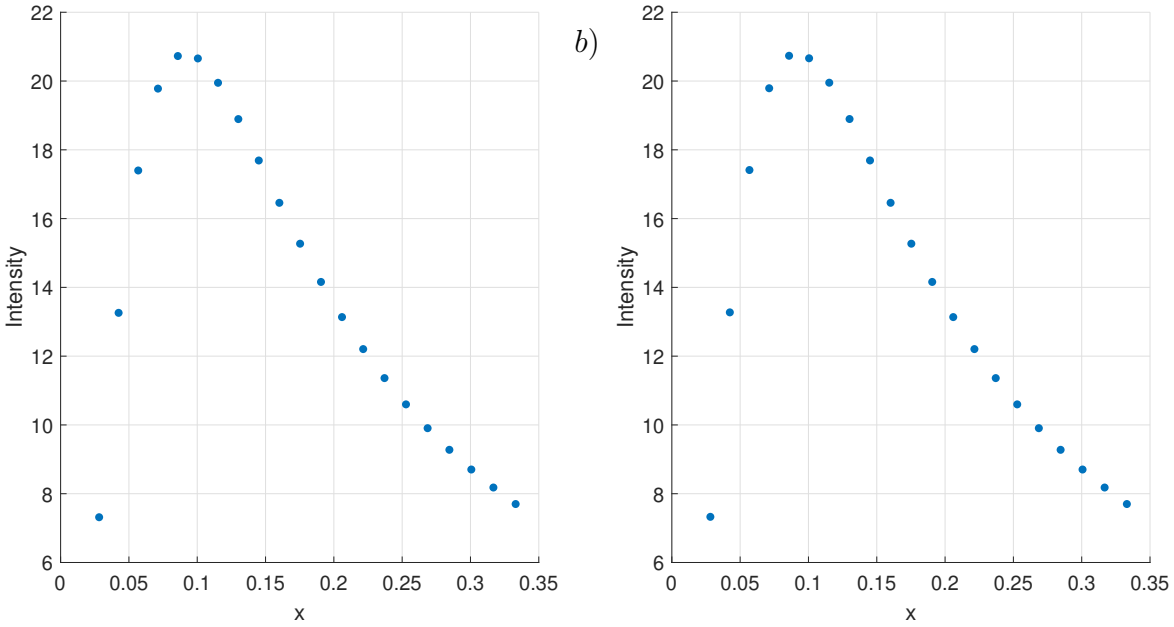

Figure 4.14: Sum of forces at the final time point in a double-layer sheet with a Newtonian layer and viscoelastic layer properties $\eta_r = 4$, $De = 0.5$, and $\mathcal{H} = 0.15$. a) Sum of forces on the Newtonian layer. b) Sum of forces on the viscoelastic layer.

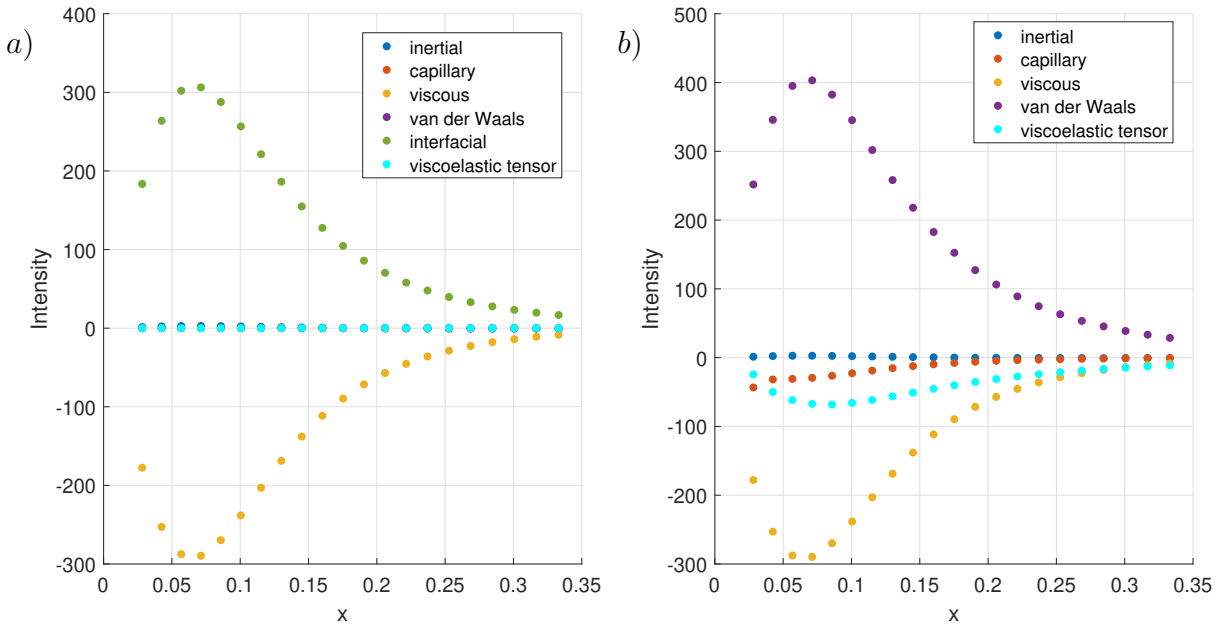

Figure 4.15: Individual forces at the final time point in a double-layer sheet with a Newtonian layer and viscoelastic layer properties $\eta_r = 4$, $De = 0.5$, and $\mathcal{H} = 0.15$. a) Individual forces on the Newtonian layer. b) Individual forces on the viscoelastic layer.

4.3.4 Maximum thickness reduction

The results presented in the previous subsections indicate that the addition of an extra layer of a viscoelastic liquid may allow a reduction in total thickness of stable liquid sheets. Here, we investigate how the reduction happens. We analyze sheet thickness reduction for different values of γ, presented in Equation (4-2), and different viscoelastic forces, characterized by η_r. From the non-dimensional coefficients definition, presented in Section 2.6, the ratio S/A is defined as

$$\frac{S}{A} = \frac{\sigma H^4 \pi}{A_0 L^2}, \tag{4-6}$$

where H is the dimensional sheet thickness. Therefore, the variation in γ represents different sheet thickness since the σ, A_0, and L remain constant. Then, higher γ indicates the curtain is thicker. First, it is simulated the rupture time of Newtonian single layers for each of the S/A ratios to be used as a reference. Then, we compute the rupture time for double sheets composed of Newtonian–viscoelastic layers with reduced thickness. The dimesnional thickness reduction, H reduction, is performed by multiplying γ by $(1-\zeta)^4$, see Equation (4-6), where ζ is the percentage reduction in dimensional thickness. Sheet rupture happens when the rupture time is shorter than the perturbation

residence time on the curtain. The maximum reduction possible, ζ_{max}, is calculated considering the reference rupture time. As it is stated in previous Subsections, the addition of an extra viscoelastic layer delays the sheet breakup time. So, this time buffer to the rupture moment can be leveraged by reducing the curtain thickness. Therefore, ζ_{max} is defined when the double layer system rupture time matches the reference single sheet rupture time. Figure 4.16 shows the results for maximum reduction percentage for all cases. We found that for higher S/A ratios, the potential reduction in sheet thickness is weaker. In a physical setting, the need for higher S/A ratios may be related to lengthier sheets, since disturbances that appear on the sheet surface take longer to get to the sheet's end. On the other hand, the increase in the non-Newtonian characteristic in the viscoelastic layer increases the maximum value for possible thickness reduction. Karim et al. [13] found experimentally the same behavior regarding the viscoelastic effects reported. They simulated the viscoelastic coating fluid as an aqueous solution of polyethylene oxide. The viscoelastic effects were tuned by changing the polymer concentration in the solution.

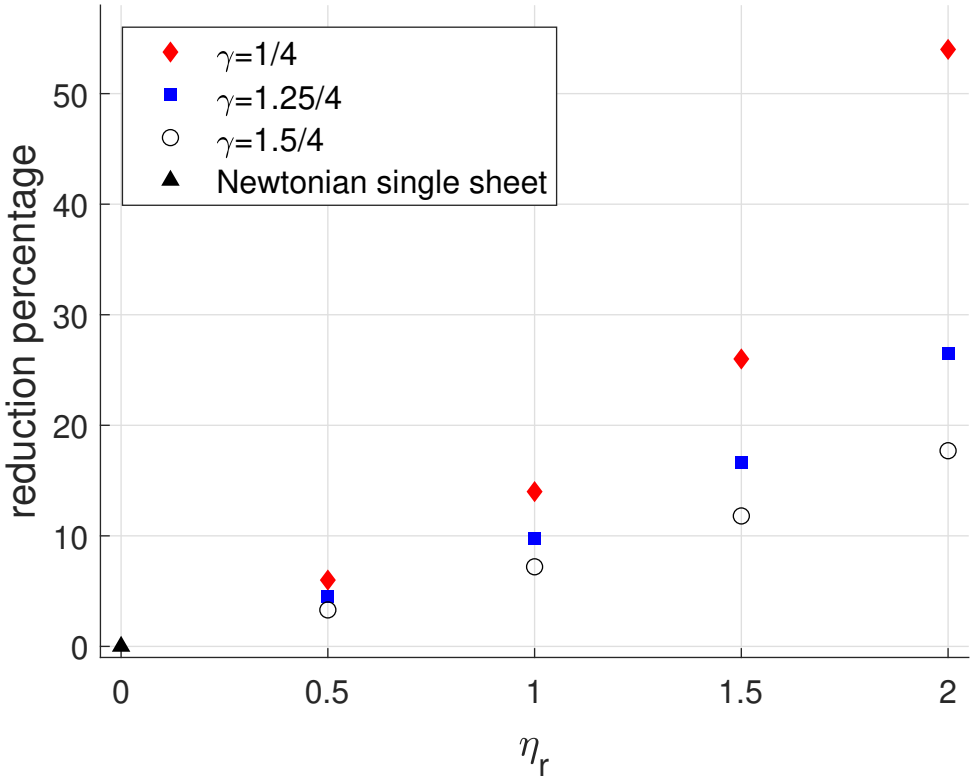

Figure 4.16: Reduction percentage on the dimensional thickness varying the γ and η_r parameters. The De parameter is set as a constant $De = 0.25$. The thickness of a single-layered Newtonian sheet is considered for reference, $\mu = 1$ mPa.s. The reduction bases on a comparison between the reference and the value for a viscoelastic-Newtonian double layer.

5
Final Remarks

It was examined the evolution of a double-layer thin-film sheet under unstable conditions until its rupture. The investigation was performed applying a numerical solver for the developed equation system describing the problem.

It was explored double-layers varying thickness ratios among a sheet composed of Newtonian and viscoelastic layers. As formerly presented by Bazzi et al. [19], the viscoelastic effect has considerable influence delaying rupture times in thin-film single sheets. The solutions obtained demonstrate that this effect is inherited in the double-layered sheets. The achieved answers show that the evolution on a double-layer with one viscoelastic layer requires more time to breakup than on a Newtonian liquid single-layer. The flow resistance effect that appears on the Newtonian layer and induced by the viscoelastic layer originates from the interfacial forces that appear on the layers' interface. Those results can explain some previously reported experimental observations on stability and thickness reduction of thin-films. Finally, it is performed simulations on dimensional thickness reduction based on the addition of a viscoelastic second layer. Those results reveal the effects of viscoelasticity and curtain length variation on the maximum reduction achievable. The model presented can be used in the design of optimal conditions for curtain coating with the goal of reducing the minimum thickness possible.

Bibliography

[1] MARTIN, P. M.. **Handbook of deposition technologies for films and coatings: science, applications and technology**. William Andrew, 2009.

[2] **Tse troller – coating secret**. `https://www.tse-coating.ch/?lang=en`. Accessed: 2021-05-11.

[3] ORON, A.; DAVIS, S. H. ; BANKOFF, S. G.. **Long-scale evolution of thin liquid films**. Reviews of modern physics, 69(3):931, 1997.

[4] BANDYOPADHYAY, D.; GULABANI, R. ; SHARMA, A.. **Instability and dynamics of thin liquid bilayers**. Industrial & engineering chemistry research, 44(5):1259–1272, 2005.

[5] POTOTSKY, A.; BESTEHORN, M.; MERKT, D. ; THIELE, U.. **Alternative pathways of dewetting for a thin liquid two-layer film**. Physical Review E, 70(2):025201, 2004.

[6] MERKT, D.; POTOTSKY, A.; BESTEHORN, M. ; THIELE, U.. **Long-wave theory of bounded two-layer films with a free liquid–liquid interface: short-and long-time evolution**. Physics of Fluids, 17(6):064104, 2005.

[7] ANTURKAR, N. R.; PAPANASTASIOU, T. C. ; WILKES, J. O.. **Lubrication theory for n-layer thin-film flow with applications to multilayer extrusion and coating**. Chemical engineering science, 45(11):3271–3282, 1990.

[8] BROWN, D.. **A study of the behaviour of a thin sheet of moving liquid**. Journal of fluid mechanics, 10(2):297–305, 1961.

[9] LIN, S.; ROBERTS, G.. **Waves in a viscous liquid curtain**. Journal of Fluid Mechanics, 112:443–458, 1981.

[10] LIN, S.. **Stability of a viscous liquid curtain**. Journal of Fluid Mechanics, 104:111–118, 1981.

[11] FINNICUM, D. S.; WEINSTEIN, S. J. ; RUSCHAK, K. J.. **The effect of applied pressure on the shape of a two-dimensional liquid curtain falling under the influence of gravity**. Journal of fluid mechanics, 255:647–665, 1993.

[12] ROCHE, J.; LE GRAND, N.; BRUNET, P.; LEBON, L. ; LIMAT, L.. **Pertubations on a liquid curtain near break-up: Wakes and free edges**. Physics of fluids, 18(8):082101, 2006.

[13] KARIM, A. M.; SUSZYNSKI, W. J.; PUJARI, S.; FRANCIS, L. F. ; CARVALHO, M. S.. **Delaying breakup and avoiding air entrainment in curtain coating using a two-layer liquid structure**. Chemical Engineering Science, 213:115376, 2020.

[14] ERNEUX, T.; DAVIS, S. H.. **Nonlinear rupture of free films**. Physics of Fluids A: Fluid Dynamics, 5(5):1117–1122, 1993.

[15] IDA, M. P.; MIKSIS, M. J.. **Thin film rupture**. Applied Mathematics Letters, 9(3):35–40, 1996.

[16] BECERRA, M.; CARVALHO, M. S.. **Stability of viscoelastic liquid curtain**. Chemical Engineering and Processing: Process Intensification, 50(5-6):445–449, 2011.

[17] SÜNDERHAUF, G.; RASZILLIER, H. ; DURST, F.. **The retraction of the edge of a planar liquid sheet**. Physics of Fluids, 14(1):198–208, 2002.

[18] MARSTON, J.; THORODDSEN, S. T.; THOMPSON, J.; BLYTH, M. G.; HENRY, D. ; UDDIN, J.. **Experimental investigation of hysteresis in the break-up of liquid curtains**. Chemical Engineering Science, 117:248–263, 2014.

[19] BAZZI, M.; CARVALHO, M.. **Effect of viscoelasticity on liquid sheet rupture**. Journal of Non-Newtonian Fluid Mechanics, 264:107–116, 2019.

[20] DINKGREVE, M.. **Uva-dare (digital academic repository) the rheology of jamming**. 2017.

[21] BARNES, H. A.; HUTTON, J. F. ; WALTERS, K.. **An introduction to rheology**, volumen 3. Elsevier, 1989.

[22] LARSON, R. G.. **Constitutive equations for polymer melts and solutions**.

[23] OLDROYD, J.. **Non-newtonian effects in steady motion of some idealized elastico-viscous liquids**. Proceedings of the Royal Society of London. Series A. Mathematical and Physical Sciences, 245(1241):278–297, 1958.

[24] IRGENS, F.. **Continuum mechanics**. Springer Science & Business Media, 2008.

[25] OLDROYD, J. G.. **On the formulation of rheological equations of state**. Proceedings of the Royal Society of London. Series A. Mathematical and Physical Sciences, 200(1063):523–541, 1950.

[26] TIRTAATMADJA, V.; SRIDHAR, T.. **A filament stretching device for measurement of extensional viscosity**. Journal of Rheology, 37(6):1081–1102, 1993.

[27] NGUYEN, D.; GUPTA, R. ; SRIDHAR, T.. **Experimental results and constitutive modelling of the extensional flow of m1**. Journal of non-newtonian fluid mechanics, 35(2-3):207–214, 1990.

[28] CARMO, M.. **Differential Geometry of Curves and Surfaces**. Prentice-Hall, 2016.

[29] STEWART, P. S.; FENG, J.; KIMPTON, L. S.; GRIFFITHS, I. M. ; STONE, H. A.. **Stability of a bi-layer free film: simultaneous or individual rupture events?** Journal of Fluid Mechanics, 777:27–49, 2015.

[30] SAVVA, N.; BUSH, J. W.. **Viscous sheet retraction**. 2009.

[31] MAZUMDER, S.. **Numerical methods for partial differential equations: finite difference and finite volume methods**. Academic Press, 2015.

[32] FERZIGER, J. H.; PERIĆ, M. ; STREET, R. L.. **Computational methods for fluid dynamics**, volumen 3. Springer, 2002.

[33] BAZZI, M. S.. **Breakup dynamics of non-Newtonian liquid sheets**. PhD thesis, PUC-Rio, 2018.